

Contributions to precision and accuracy of monazite microprobe ages

JOSEPH M. PYLE,^{*,1} FRANK S. SPEAR,¹ DAVID A. WARK,¹ CHRISTOPHER G. DANIEL,²
AND LARA C. STORM¹

¹Department of Earth and Environmental Sciences, Rensselaer Polytechnic Institute, Troy, New York 12180-3590, U.S.A.

²Department of Geology, Bucknell University, Lewisburg, Pennsylvania 17837, U.S.A.

ABSTRACT

We examine the factors controlling accuracy and precision of monazite microprobe ages, using a JEOL 733 Superprobe equipped with 4 PET crystals, and both 1-atm gas flow Ar X-ray detectors and sealed Xe X-ray detectors. Multiple PET crystals allow for simultaneous determination of Pb concentration on up to 3 detectors, and the effects of different detector gases on spectral form can be addressed. Numerous factors in the X-ray production, detection, and counting sequence affect spectral form, including: choice of accelerating voltage, changes in *d*-spacing of the diffraction crystal, use of X-ray collimation slits, and type of detector gas. The energy difference between ArK α X-rays and XeL α X-rays results in, for 1-atm Ar detectors, escape peaks of second-order LREE *L* line X-rays that cannot be filtered using differential mode PHA. The second-order LREE energies are passed to the counter and produce, for a 140 mm Rowland circle, several problematic interferences in the Pb region of a monazite wavelength-dispersive (WD) spectrum. WD monazite spectra produced with Xe detectors are free from second-order LREE interferences in the Pb region; escape peaks of the second-order LREE are filterable with differential mode PHA if Xe detectors are employed.

Silicon, Ca, Y, Ce, P, Th, U, and Pb (2 spectrometers) are measured as part of the monazite microprobe dating protocol; $\pm 2\sigma$ variations in elements fixed for ZAF corrections do not affect the age outside of analytical uncertainty. ThM α , UM β , and PbM α are the analyzed lines of the age components. Corrections for interference of ThM $\zeta_{1,2}$ and YL $\gamma_{2,3}$ on PbM α are significant, but can be done precisely, and reduce the precision of the M α analysis by a trivially small amount. ThM γ , M3-N4, and M5-P3 interferences on UM β can be corrected, as well, but ThM5 and M4 absorption edges in high-Th samples make estimation of UM β background problematic. Background fits for UM β peaks show that linear vs. exponential fits for UM β do not, in general, produce statistically significant differences in microprobe ages. However, linear vs. exponential background fits for PbM α peaks do produce significantly different ages, most likely because of (1) low Pb concentrations relative to U; (2) ThM ζ_1 interference on backgrounds between ThM ζ_1 and PbM β ; and (3) SK α and K β interference in S-bearing monazite.

For 6-min analyses (3 min peak, 3 min background) at 25 keV and 200 nA, 1 σ Pb precisions are approximately 3–4% at 1700 ppm and 9.5% at 750 ppm; at 15 keV, precision decreases by roughly 25% of the 25 keV value. These precisions are constant for fixed current, analysis time, and concentration, but the statistical precision of distinct populations of monazite grains (domains) is a function of the total number of analyses within the domain. Instrumental errors (current measurement, dead time, pulse shift, *d*-spacing change) add 1–10% to random errors, but errors caused by pulse shift and *d*-spacing changes can be accounted for and corrected. Decreasing accelerating voltage from 25 to 15 keV decreases ZAF correction factors by as much as 50% relative, but replicate age analyses of Trebilcock monazite at 15 and 25 keV are statistically indistinguishable. Grain orientation, miscalculated background intensity, uncorrected interferences, and surface effects also introduce systematic errors. Accurate background interpolation and interference correction reduces systematic error to approximately 5–20% in addition to random (counting) error.

Microprobe ages (~420 Ma) and ²⁰⁸Pb/²³²Th SIMS ages (~430 Ma) of monazite from Vermont are in agreement to within ~10 m.y. The discrepancy between U-Th-total Pb microprobe ages and ²⁰⁸Pb/²³²Th ages is removed when the high background measurement for PbM α is shifted to the short-wavelength side of PbM β , removing a possible ThM ζ_1 interference.

INTRODUCTION

The recognition by Parrish (1990) that monazite incorporates little common Pb spurred investigators to attempt in-situ dating

* E-mail: pylej@rpi.edu

of monazite with the electron microprobe analyzer (EMPA). Monazite is an ideal candidate for mineral dating; in addition to excluding common Pb, it can incorporate significant amounts of Th and U (Spear and Pyle 2002, and references therein), leading to accumulation of measurable amounts of radiogenic Pb in as

little as 50–150 million years. Diffusion of Pb in monazite is negligible (Cherniak et al. 2004); for a cooling rate of 10 °C/m.y., the Pb closure temperature for a 10 µm grain is approximately 900 °C. Monazite is also highly resistant to metamictization (Karioris et al. 1991; Meldrum et al. 1997), so the probability of Pb loss due to accumulated lattice damage is small.

Suzuki and Adachi (1991) and Suzuki et al. (1994) pioneered EMPA dating of monazite with the CHEMical Isochron METHod (CHIME). Single-point monazite ages and statistical treatment of these ages were addressed by Montel et al. (1996), using the methods of Wendt and Carl (1991). Williams et al. (1999) produced the first monazite age maps by running background-subtracted U, Th, and Pb pixel values through the monazite age equation (e.g., Montel et al. 1996):

$$\text{Pb} = \text{Th}/232 \left[e^{\lambda^{232t}} - 1 \right] 208 + (U/238.04) 0.9928 \times \left[e^{\lambda^{238t}} - 1 \right] 206 + (U/238.04) 0.0072 \times \left[e^{\lambda^{235t}} - 1 \right] 207 \quad (1)$$

The abundance of EMPAs relative to in-situ isotopic analyzers has led to a proliferation of microprobe monazite ages for both ancient and recent plutonism, sedimentation, deformational episodes, and metamorphic reactions (e.g., Kim et al. 1997; Pan and Stauffer 2000; Cho et al. 1999; Grew et al. 2001; Asami et al. 2002; Krohe and Wawrzenitz 2000; Williams and Jercinovic 2002; Pyle and Spear 2003). Despite the apparent simplicity of the method, EMPA dating of monazite is beset by several uncertainties and difficulties, making a rigorous assessment of the accuracy and precision associated with each age a non-trivial task. Sources of error are introduced at several stages of the analytical process, including sample preparation, calibration, analysis, and post-analysis data reduction (e.g., Scherrer et al. 2000).

Maximizing precision and accuracy is the primary goal of each monazite age determination. Compromising the success of this simply stated goal is the recognition that variation in monazite grain size, orientation, textural setting, and compositional or age zoning may preclude the development of a single monazite EMPA dating protocol. In this paper, we discuss optimization of the analytical precision of Pb and other elements critical to microprobe dating of monazite. The processes of X-ray generation, detection, and spectral refinement are examined with respect to EMPA artifacts capable of affecting the precision and accuracy of U, Th, and Pb measurement. Additionally, instrumental and specimen errors are quantified in terms of resulting compositional and age variation. Replicate analyses, using a variety of dating protocols, are presented for monazite of variable age and composition. Appendices include (1) a derivation of the statistical precision of U and Pb analyses corrected for elemental interference, and (2) a complete analytical protocol for microprobe age analysis of monazite.

EMPA HARDWARE

Variations in EMPA electron column, spectrometers, X-ray detectors, and counters can have profound effects on the form of wavelength-dispersive spectra, the resultant concentrations of U, Th, and Pb, and the calculated age. Though many of the concepts discussed here are applicable universally, monazite dating protocols must be developed with a specific EMPA in mind, as hardware differences from machine to machine preclude universal application of a single dating protocol.

All experiments and results presented in this paper utilized a JEOL 733 Super-

probe (hereafter referred to as the 733) manufactured in 1985. The 733 employs a tungsten filament, and can access beam energies of 1–35 keV and beam currents of ~50 pA to 2.0 µA, with beam diameters adjustable between 1 and 50 µm. The central column has an X-ray takeoff angle of 40°, and is surrounded by 5 wavelength-dispersive spectrometers, the configurations of which are listed in Table 1.

All spectrometers in the 733 incorporate a 140 mm radius Rowland circle. Wavelength dispersive (WD) scans presented below are referenced to this radius (R_R), such that, for all WD scans,

$$L_{\text{PET}} \text{ (in mm)} = (R_R/d_{\text{PET}}) \times n\lambda_i, \quad (2)$$

where d_{PET} is the d -spacing of the PET (002 pentaerythritol) diffraction crystal (8.74 Å), n is the order of the X-ray line i , and λ_i is the wavelength (in angstroms) of the first-order X-ray line i . Each spectrometer in the 733 is equipped with two swappable diffraction crystals. Four of the five spectrometers on the RPI 733 Superprobe are equipped with PET diffraction crystals, enabling simultaneous detection of Pb X-rays on as many as three spectrometers, with concurrent detection of U and Th on the fourth PET-bearing spectrometer.

Adjustable X-ray collimators are placed between the diffraction crystal and X-ray detector on all five spectrometers. Collimators minimize X-ray beam divergence and defocusing inherent in the Johann (1931) focusing arrangement for diffraction crystals, which is the focusing arrangement used in the 733. The X-ray collimators in the 733 are adjustable to widths of 3 mm (“open setting”), 500 µm, and 300 µm.

The 733 incorporates P10 (Ar 90%-CH₄ 10%) gas-flow X-ray detectors with spectrometers 1–3 and Xe-CO₂ sealed X-ray detectors with spectrometers 4 and 5; Polypropylene entry windows are used on the gas-flow detectors, and Be windows are used with sealed detectors. Gas pressure in the flow detectors is maintained at approximately 1 atm (~760 torr), and P_{Xe} in the sealed detectors is on the order of 10–60 torr.

Variability in EMPA hardware directly affects the accuracy of measurement of elements critical to monazite microprobe dating. Some examples of hardware variability are listed in Table 1, along with a brief description of the ensuing effects. Although the same types of responses can occur in any EMPA, it is emphasized that the spectral responses presented in this paper are specific to the 733, and arise from the combination of individual hardware components that constitute the EMPA used in this study. Variability in EMPA hardware, and resulting differences in spectral acquisition and measurement of intensity are discussed, where appropriate, in the body of the text. It should be borne in mind that understanding the precision limitations of a particular EMPA will ultimately reveal, and limit, the types of geochronologic, petrogenetic, and tectonic questions that may be answered with microprobe age data.

X-RAY GENERATION-PROCESSING PATH IN THE EMPA, AND EFFECTS ON WD SPECTRA AND MEASURED INTENSITY

Accelerating voltage and electron beam-sample interaction

The choice of accelerating voltage is influenced primarily by the energy required to excite selected characteristic X-ray lines. Accelerating voltage settings from published monazite literature (summarized in Scherrer et al. 2000) range from 15 to 25 keV; the value selected should be, at a minimum, 2–3 times the critical excitation energy of the analyzed characteristic X-ray (Scott et al. 1995). Additionally, higher accelerating voltages increase the intensity of generated X-rays, resulting in greater analytical precision for a given analysis current and duration. Although higher analytical precision is favored in microprobe monazite dating, two hazards of adopting high (25 keV) vs. low (15 keV) accelerating voltages exist: (1) increased X-ray excitation volume within the sample, and (2) increased uncertainty in ZAF corrections. Quantitative aspects of ZAF corrections at 15 vs. 25 keV are addressed in the section on accuracy of age determinations.

Figure 1 shows an Electron Flight Simulator (Small World, Inc.) Monte Carlo simulation (10000 trials) of the electron interaction and X-ray generation volumes for CeLα, ThMα, UMa,

TABLE 1A. JEOL 733 Superprobe hardware: 733 configuration

Spectrometer	1	2	3	4	5
Radius (mm)	140	140	140	140	140
Collimating slit?	yes	yes	yes	yes	yes
Column-spectrometer separation?	no	no	no	no	no
Diffraction crystal	LDE1/TAP	STE/PET	TAPJ/PETJ	PET/LiF	PET/LiF
Detector type	Gas flow	Gas flow	Gas flow	sealed	sealed
Entry window configuration	Side – 24 x 1.5 mm				
Entry window material	polypropylene	polypropylene	polypropylene	beryllium	beryllium
Exit window	none	none	none	none	none
Detector gas	P10	P10	P10	Xe-CO ₂	Xe-CO ₂
Gas pressure	~760 torr	~760 torr	~760 torr	10-60 torr P_{Xe}	10-60 torr P_{Xe}

TABLE 1B. JEOL 733 Superprobe hardware: EMPA hardware variability

Hardware	Variability	Effects
Rowland circle	160 mm radius	-better spectral resolution -lower X-ray intensity
Rowland circle	100 mm radius	-poorer spectral resolution -higher X-ray intensity
diffraction crystal (PET)	larger surface area	-higher x-ray intensity relative to small crystals -imperfections more prevalent in large crystals, specular effects leading to spectral anomalies
detector windows	increased size	-increased detector efficiency -greater chance of failure
detector exit windows	presence/absence	-affects range of X-ray energies accessed by counter
collimation slits	presence/absence	-presence decreases specular defocusing, increases P/B ratio -presence decreases X-ray intensity
spectrometer-column separation	presence/absence	-presence lessens likelihood of crystal/detector contamination -presence minimizes detector gas leakage effects -presence results in higher pressure in spectrometers relative to column
gas-flow detectors	pressure of detector gas	-presence causes some absorption of X-rays in column volume -increasing pressure lowers absorption edge and escape peak intensity -increasing pressure results in large spectrometer chamber-detector pressure differential

and $PbM\alpha$ at 15 keV (Figs. 1a–1e) and 25 keV (Figs 1f–1j). Two monazite compositions are modeled, a moderate-Th monazite $[La_{0.225}Ce_{0.495}Nd_{0.18}(CaTh)_{0.09}(CaU)_{0.007}(PbTh)_{0.003}PO_4, \rho = 4.72, Z = 57.84]$ and a Th-rich monazite $[La_{0.1875}Ce_{0.4125}Nd_{0.15}(CaTh)_{0.24}(CaU)_{0.007}(PbTh)_{0.003}PO_4, \rho = 5.03, Z = 63.13]$. No significant differences between the X-ray simulations were noted for the two compositions; the moderate-Th monazite is shown in Figure 1.

The electron interaction volume and X-ray generation volumes have roughly equal radii at 15 keV (~1 μm). At 25 keV, the e^- interaction and X-ray generation volumes increase to a radius of ~3 μm , except for $ThM\alpha$, which has a slightly smaller generation volume ($R \sim 2 \mu m$). The simulation suggests that 25 keV accelerating voltages may cause generation of X-rays in multiple compositional domains if the compositional domains have effective radii $\leq 3 \mu m$. Mapping of compositional domains in monazite (e.g., Williams et al. 1999; Pyle and Spear 2003) commonly reveals compositional domains of this size or smaller. As different elements possess different excitation volumes, the X-rays of one element may sample two domains, while the X-rays from another element may be generated within a single domain. Additionally, monazite rim analyses at 25 keV run a greater risk of exciting X-rays in surrounding phases, or the mounting medium for analyses of mineral separates.

Any edge analysis can be influenced by spectrometer orientation. Additionally, subsurface inclusions, or compositional heterogeneities smaller than electron-beam resolution will also affect microprobe age analyses. Figure 2 shows a schematic cross section of an inclusion-bearing monazite grain and adjacent

matrix phases. The two monochrometers (diffraction crystals) are separated by an angle of approximately 180°. Electron beam 1 generates excitation volume 1, and X-rays from volume 1 reaching monochromer B1 pass entirely through monazite, whereas X-rays reaching monochromer A1 pass largely through the adjacent grain. Common pelite phases such as quartz, micas, and plagioclase have atomic numbers and mass-absorption coefficients markedly different from monazite. As a result, the diffracted X-rays (U, Th, Pb) will be corrected for monazite atomic number and mass absorption effects, when in fact, the atomic number and mass-absorption corrections for the matrix phase should apply. Likewise, X-rays from excitation volume 2 reaching monochromer A2 will pass largely through monazite, whereas the X-rays reaching monochromer B2 will pass largely through the subsurface inclusion in monazite, once again rendering ZAF correction factors for monazite non-applicable. A specific example of this effect is presented in the section addressing specimen errors.

X-ray-diffraction crystal interactions

Upon exiting the sample volume, the X-rays fan out toward a diffraction crystal, where X-rays of a wavelength satisfying the Bragg equation are diffracted by the crystal and travel to the X-ray detector. Two types of spectrometer focusing arrangements are used in EMPAs, with each utilizing the diffraction crystal in different ways. The focusing arrangements are Johannson (1933) focusing, and Johann (1931) focusing.

To minimize Bragg angle defocusing that are inherent in

the Johann (1931) focusing arrangement, X-ray collimator slits may be placed between the sample and the diffraction crystal, or between the diffraction crystal and the X-ray detector (as is the case in the 733). In this study, we found no significant difference in U, Th, or Pb peak-to-background ratios for different collimator widths, and we adopted an open (3 mm) collimator setting for all tests and age analyses.

PET diffraction crystals (used for Pb, Th, and U analysis) are prone to thermal expansion. Jenkins and DeVries (1982) show that significant thermal expansion of PET can occur for

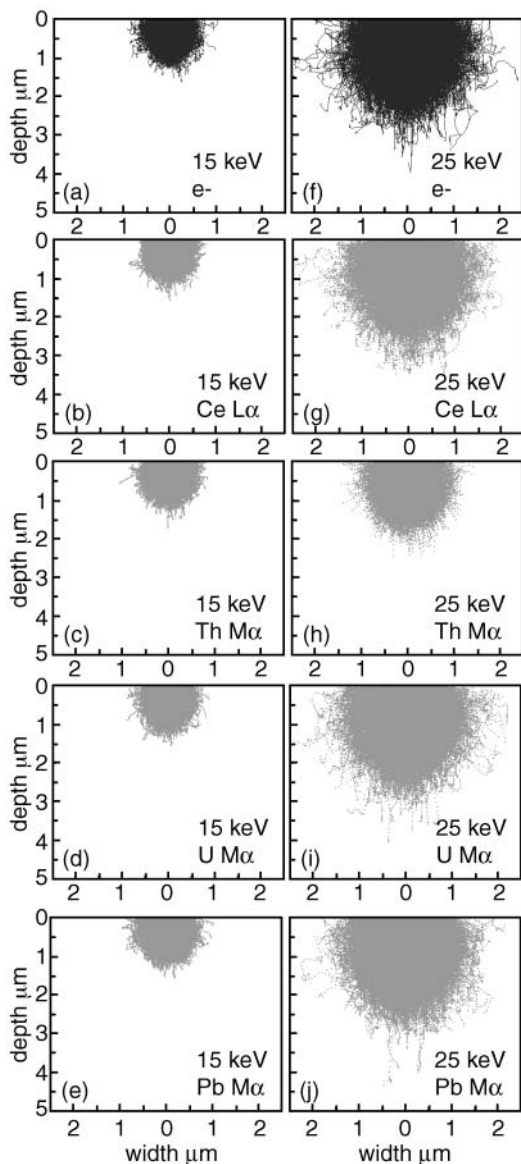


FIGURE 1. Monte Carlo simulations of the interaction volumes of electrons and generation volumes of X-rays at 15 keV (a–e) and 25 keV (f–j) for $CeL\alpha$ (b, g), $ThM\alpha$ (c, h), $UM\alpha$ (d, i), and $PbM\alpha$ (e, j). Simulation was performed with Electron Flight Simulator™ (Small World, Inc.) and consists of 10,000 trials. Monazites of composition $(La_{0.225}Ce_{0.495}Nd_{0.18}(CaTh)_{0.09}(CaU)_{0.007}(PbTh)_{0.003}PO_4, (\rho = 4.72, Z = 57.84))$ and $(La_{0.1875}Ce_{0.4125}Nd_{0.15}(CaTh)_{0.24}(CaU)_{0.007}(PbTh)_{0.003}PO_4, \rho = 5.03, Z = 63.13)$ produce no discernable difference in excitation volume.

even modest temperature changes (Fig. 3). $PbM\alpha$, at a 2θ of approximately 74.4° for PET, is particularly prone to peak shift; a change of $5^\circ C$ in ambient temperature results in a calculated peak shift of about $0.05^\circ 2\theta$. This angular change translates to a peak shift of approximately $D_{Rowland}$ of 0.15 mm, and, as measured on the JEOL 733, a loss of approximately 20% of previous peak counts. Decreases of 3–7% in Pb k -ratio during analysis indicate a temperature shift on the order of 1–2 $^\circ C$. This observation underscores the importance of climate control in the space housing any EMPA used for dating monazite.

X-ray detector and counter

Two of the PET crystals in the 733 are combined with gas-flow (P10) X-ray detectors; the other two PET crystals are used in conjunction with sealed (Xe) X-ray detectors. P10 in the gas-flow detectors is maintained at approximately 1 atm, and the partial pressure of Xe in the sealed detectors is approximately 10–60 torr (Geller and Herrington 2002). This configuration lends itself to an examination of the effect of detector gas on the WD spectrum.

Figure 4 shows a single-channel analyzer (SCA) scan of $CePO_4$ containing 1.5 wt% Pb. The figure shows the scan with the spectrometer tuned to $CeL\alpha$ ($n = 2$) (Fig. 4a) and $PbM\beta$ (Fig

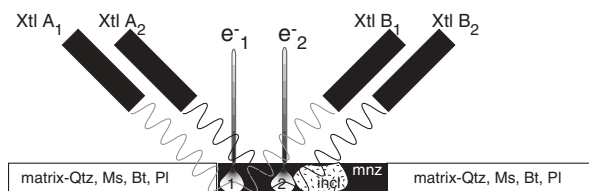


FIGURE 2. Schematic of emergent X-rays produced during monazite analysis. Two X-ray production volumes are indicated by teardrop-shaped cross-sections. X-rays from excitation volume 1 are diffracted by monochrometers A1 and B1, and X-rays from excitation volume 2 are diffracted by monochrometers A2 and B2. X-rays diffracted by different monochrometers may sample X-rays that have passed through areas of highly different composition (zonal domains), atomic number, and/or absorption potential (adjacent grains or micro-inclusions), resulting in significantly different calculated element concentrations.

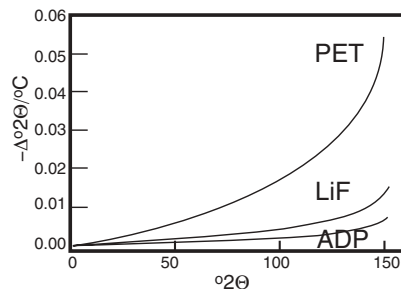


FIGURE 3. Plot of change in diffraction crystal 2θ angle as a function of temperature (Jenkins and DeVries 1982). Diffraction crystals shown are LiF, ADP, and PET. PET is particularly sensitive to temperature changes. $PbM\alpha$ measured on PET has a 2θ angle of 77.4° . A change in ambient temperature of $5^\circ C$ results in a $PbM\alpha$ $\Delta 2\theta$ of 0.025° , which translates to a loss of approximately 20% of $PbM\alpha$ counts, as measured on the JEOL 733.

4b). With the spectrometer tuned to the $CeL\alpha$ ($n = 2$) peak, the voltage pulse from the second order $CeL\alpha$ peak is visible, as is the $CeL\alpha$ ($n = 2$) escape peak. When the spectrometer is tuned to $PbM\beta$ (Fig. 4b), imperfect focusing of the diffraction crystal results in detection of several $CeL\alpha$ ($n = 2$) X-rays. The diminished voltage pulse from $CeL\alpha$ ($n = 2$) is visible, but the $CeL\alpha$ ($n = 2$) escape peak is overlapped by the voltage pulse from the more intense $PbM\beta$ peak.

The energy difference between escape peaks formed in Ar vs. Xe detectors has a profound effect on the form of the pulse-height distribution of lead. Lead M lines have energies of 2.345 keV ($PbM\alpha$) and 2.442 keV ($PbM\beta$), respectively. Typically, the most abundant elements in monazite (besides P) are the LREE La, Ce, and Nd, which have $L\alpha_1$ energies between 4.65–5.23 keV, and $L\beta_1$ energies between 5.04–5.72 keV. Subtracting the energy of the $ArK\alpha$ line from the energies of the LREE $L\alpha$ and $L\beta$ lines results in energies for LREE $L\alpha$ and $L\beta$ escape peaks between 1.69–2.76 keV. This energy range overlaps the characteristic energies of $PbM\alpha$ and $PbM\beta$. The maximum difference between the Pb M line energies and LREE $L\alpha$ and $L\beta$ escape peak energies is <0.8 keV, and the minimum difference is approximately 0.05 keV. The energy of $XeL\alpha$ X-rays (4.11 keV) is greater than that of $ArK\alpha$ X-rays. Consequently, there is a larger difference between the energies of LREE escape peaks formed in a Xe detector and the Pb M lines. For LREE_{Esc,Xe} – Pb M , the energy difference is 0.75–1.90 keV, significantly larger than the equivalent energy difference in Ar detectors.

The X-ray lines that generate escape peaks problematic to Pb analysis are the second- and third-order lines of the abundant REEs in monazite: La, Ce, Nd, and, to a lesser extent, Pr, Sm, and Gd. If pulse-height discriminators are in integral mode, these lines will appear, at full intensity, in the region of interest for Pb peak and background count collection—roughly 190 to 150 mm on a PET crystal with a 140 mm Rowland Circle. Use

of differential-mode, pulse-height discriminators will filter the energies from these higher-order lines; the remaining intensity appearing on a WD spectrum is due to the escape peaks.

The formation and distribution of escape peaks in pulse-height analyzers, and their effect on the appearance of WD spectra, can be assessed with a virtual wavelength-dispersive analysis program, such as Virtual WDS (Reed and Buckley 1996). Figure 5 shows virtual pulse-height scans generated for Pb-doped (0.5 wt%) $CePO_4$, for both Ar (Fig. 5a) and Xe detectors (Fig. 5b) with the spectrometer tuned to the $PbM\beta$ peak. Several monazite microprobe-dating protocols (e.g., Scherrer et al. 2000) select $PbM\beta$ for analysis over $PbM\alpha$ due to the absence of significant element interferences, namely $ThM\zeta_1$, $ThM\zeta_2$, and $YL\gamma_{2,3}$. Two points here warrant discussion. First, the Ar escape peak from the second-order $CeL\alpha_1$ line falls largely within the voltage window occupied by $PbM\beta$ (Fig. 5a), whereas the $CeL\alpha$ ($n=2$) escape peak in the Xe detector is completely excluded by the voltage window centered on $PbM\beta$. Second, the intensity of the escape peak in the Xe detector is much less than that of the Ar detector escape peak. Xenon detector escape peaks have, in general, lower intensities than Ar detector escape peaks (Scott et al. 1995) because: (1) the K -absorption edge of Xe is at much higher energy (34.56 keV) than the range of energies (0–25 keV) encountered in typical EMP analysis; and (2) $XeL\alpha$ X-rays are more efficiently absorbed in Xe gas than are $ArK\alpha$ X-rays in Ar gas in detectors operating at 1 atm pressure. However, the quench gas type, and detector gas pressure also control escape-peak intensity, and escape-peak interferences problematic to 1-atm Ar detectors with 140 mm Rowland circles may be mitigated with a combination of a larger (160 mm) Rowland circle and high-pressure Ar X-ray detectors (Jercinovic and Williams 2005).

MEASUREMENT OF CRITICAL MONAZITE ELEMENTS IN OPTIMIZED SPECTRA

Element selection

Once X-ray detector settings have been optimized for analysis, raw elemental intensities are measured. An analytical schedule can range from a full monazite analysis routine (15–20 elements) to one that includes only the age equation components plus elements required for interference corrections. Multi-spectrometer, long-duration measurement of Pb to maximize analytical precision generally precludes simultaneous measurements of all common elements in monazite.

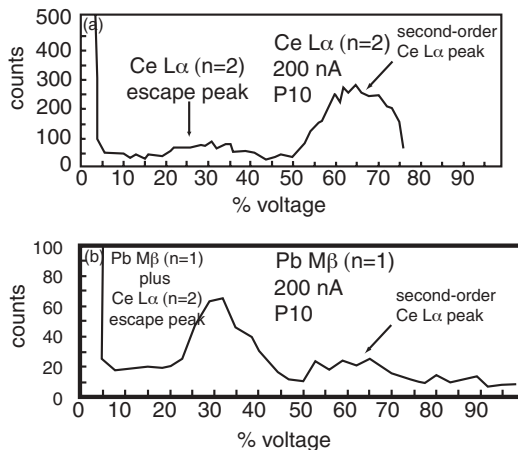


FIGURE 4. Single-channel analyzer (SCA) scans of $CePO_4$ doped with Pb. (a) Voltage scan of $CePO_4$ doped with Pb, at $CeL\alpha$ ($n = 2$) spectrometer position, showing greater pulse voltage generated by higher-order X-ray lines, as well as Ar Ce escape peak. (b) scan of material in a, with spectrometer tuned to $PbM\beta$ ($n = 1$). Limited gas ionization by $CeL\alpha$ ($n = 2$) is evident at greater voltages, but Ar Ce escape peak is masked by voltage pulse generated from $PbM\beta$ X-rays.

TABLE 2. Average pelite monazite composition (Pyle 2001) for use in ZAF correction

Oxide	Oxide wt%	1σ	Element wt%	+2σ element	-2σ element
SiO ₂	0.23	0.21	0.11	0.30	< 0
P ₂ O ₅	29.87	0.72	13.03	13.66	12.40
CaO	0.90	0.25	0.65	1.00	0.29
La ₂ O ₃	14.07	0.80	12.00	13.36	10.63
Ce ₂ O ₃	29.54	1.33	25.22	27.49	22.95
Pr ₂ O ₃	2.92	0.19	2.50	2.82	2.17
Nd ₂ O ₃	12.41	0.7	10.64	11.84	9.44
Sm ₂ O ₃	1.89	0.3	1.63	2.15	1.11
Gd ₂ O ₃	1.56	0.35	1.35	1.96	0.75
Dy ₂ O ₃	0.59	0.28	0.51	1.00	0.03

Notes: Average of 526 analyses. Elements measured in monazite chemical age analysis include Y, Si, Ca, P, Ce, Pb, U, Th, Si, Ca, P, and Ce were not measured in previous chemical dating protocols.

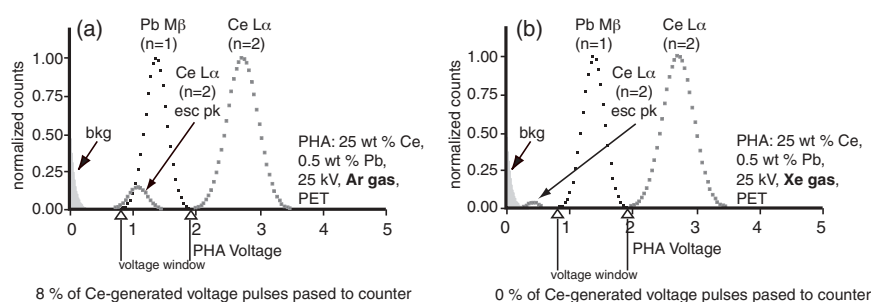


FIGURE 5. Effect of detector gas on wavelength-dispersive spectrum. (a) Virtual Pulse-Height Analyzer (VPHA; Reed and Buckley 1996) scan of Pb-bearing CePO_4 , with spectrometer set to $\text{PbM}\beta$ position. A narrow voltage window filters out the second order $\text{CeL}\alpha$ peak, but the majority of the second-order Ce escape peak falls within the voltage window set for passing the $\text{PbM}\beta$ peak. (b) VPHA scan of the same material, but using a Xe detector. The greater energy differential between the Xe absorption edge and the $\text{CeL}\alpha$ peak results in a Ce escape peak with a voltage distribution that falls outside of the voltage window.

Fixed concentrations for non-measured elements must be used for ZAF or $\phi\rho z$ corrections. The fixed values can be obtained by a full monazite analysis, or a representative set of concentrations may be used. An example of such an elemental concentration matrix is shown in Table 2 (Pyle 2001), which is an average of 526 analyses of pelitic monazite from central New England. Clearly, a wide range in monazite LREE concentration is possible, and fixed-element ZAF or $\phi\rho z$ corrections cannot accommodate such variation. If fixed concentrations are used for matrix corrections, the effect of their variations on ZAF or $\phi\rho z$ corrections must be evaluated (see section on errors).

Our analytical protocol is a compromise between full monazite analysis and analysis of the minimum number of components required for age calculation. Besides the actinides and Pb, Y, Ce, P, Ca, and Si are measured. The measurement of Ce, P, Ca, and Si (along with Th and U) encompasses all compositional variation caused by CePO_4 -huttonite and CePO_4 -brabantite exchanges. Measurement of these elements typically accounts for 65–70 wt% (on an oxide basis) of the components in monazite, and addition of fixed and measured concentrations generally yields oxide totals between 95 and 105 wt%.

Once elements are selected for measurement, the region of the WD spectra containing the characteristic peak should be examined to determine: (1) whether the α or β peak should be measured; (2) potential background collection positions; and (3) potential peak and background interferences

Xe and 1 atm Ar WD spectra—U, Th, and Pb standards

WD scans of U, Th, and Pb standard material with PET diffraction crystals on both gas-flow 1-atm Ar and sealed Xe X-ray detectors (Fig. 6) show both I_β/I_α ratios as well as diffraction crystal and detector gas influence on the absolute intensity of measured lines. Of the two Ar detectors (2,3) on the 733, one (3) is fitted with a large PET diffraction crystal (PETJ), and the result is an approximate doubling of peak intensity minus background intensity (P-B intensity) for all three elements.

For Pb (Fig. 6a) and Th (Fig. 6b), I_β/I_α is approximately 0.7, regardless of detector type. For U, however (Fig. 6c), the presence of the Ar K -absorption edge at 3.871 \AA (123.98 mm PET) between $\text{UM}\alpha$ ($3.910 \text{ \AA}/125.23 \text{ mm}$) and $\text{UM}\beta$ ($3.716 \text{ \AA}/119.02 \text{ mm}$) results in a significant increase in $\text{UM}\beta$ intensity relative

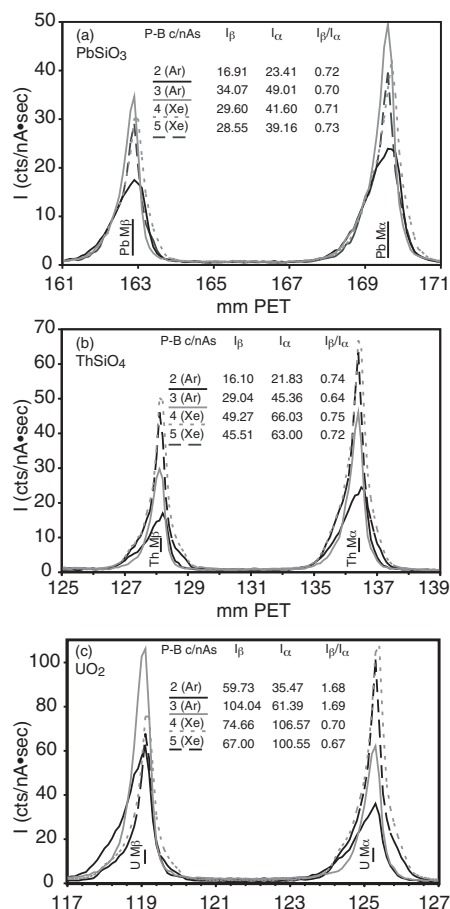


FIGURE 6. Plots of X-ray intensity (in counts/nA·s) for U, Th, and Pb calibration standards used in chemical dating of monazite. (a) synthetic PbSiO_3 , (b) synthetic ThSiO_4 , and (c) synthetic UO_2 . solid black line = intensity on spectrometer 2 (1-atm Ar detector, PET crystal); solid gray line = intensity on spectrometer 3 (1-atm Ar detector, PETJ crystal); short dashed gray line = intensity on spectrometer 4 (Xe detector, PET crystal); long dashed black line = intensity on spectrometer 5 (Xe detector, PET crystal). This and subsequent WD intensity scans plot intensity against sample-diffraction crystal distance specific to a Rowland circle of 140 mm radius.

to $UM\alpha$ intensity ($I_{\beta}/I_{\alpha} \sim 1.7$) compared to U intensity measured on Xe detectors ($I_{\beta}/I_{\alpha} \sim 0.7$). Thus, if 1-atm Ar detectors are used to measure U intensity, the raw intensity of $UM\beta$ will be greater than that of $UM\alpha$.

The precision of monazite microprobe ages is a first-order function of the precision of Th, U, and Pb analyses. Uranium and Pb are generally present in much lower abundance than Th in most (but not all) monazites (Spear and Pyle 2002, and references therein), so U and Pb analytical precision will, to a large extent, control the precision of the age estimate. Therefore, whatever combination of analytical line, diffraction crystal, and X-ray detector generate the most precise U and Pb analyses on a particular EMPA should be selected. Line selection should be assessed in an unknown for potential interference effects, which may or may not be severe enough to warrant the selection of an alternate X-ray line. A final selection of analytical lines is contingent upon the effects of analytical interferences affecting Th, U, and Pb in natural monazite.

First-order and higher-order peak and background interferences

X-ray spectral interferences may be divided into two groups: interferences caused by first-order X-ray lines, and those caused by higher-order X-ray lines. First-order interferences cannot be filtered with differential mode PHA, and require empirical or theoretical correction, or analysis of another X-ray line free from the interference in question. Additionally, the existence of first-order interferences in natural monazite, which are absent from calibration standards, may necessitate collection of background intensities for a given elemental line with one pair of background offsets (or regions) for the standard, and another pair of background offsets for the unknown. Second- and higher-order interfering X-ray lines are filterable with differential mode PHA, as long as the escape peaks of the interfering element do not produce voltage pulses that overlap the energy of the voltage pulse of the desired analyte.

In monazite, $ThM\alpha$ may be measured without interference. However, peak and background regions for both $M\alpha$ and $M\beta$ lines of Pb and U in monazite are subject to several first- and higher-order interferences. Common first- and second-order interferences for $PbM\alpha$ and $UM\beta$ in monazite are listed in Table 3. The higher resolution of a 160 mm Rowland circle (e.g., CAMECA instruments) may eliminate some of these interferences.

First-order interferences with $PbM\alpha$ include $ThM\zeta_1$, $ThM\zeta_2$, and $YL\gamma_{2,3}$. WD Scans of the $PbM\alpha$ region in $ThSiO_4$ and YPO_4 (Fig. 7a) show the intensities of these peaks, as well as their locations relative to $PbM\alpha$. Measurement of $PbM\alpha$ in monazite requires correction for interference of $ThM\zeta_1$, $ThM\zeta_2$, and $YL\gamma_{\alpha}$ (see Appendix 1). Second-order interferences on $PbM\alpha$ include $LaL\alpha$ and $ThM2-O4$, but these are of concern only on 1-atm Ar detectors.

First-order interferences occurring at potential $PbM\alpha$ background positions include $SK\alpha$, $PbM\beta$, $UM\zeta_2$, $SK\beta_1$, and $UM\zeta_1$. The second-order L family of lines of La, Ce, and Nd (particularly those listed in Table 4) are potential interferences on $PbM\alpha$ background, but only if 1-atm Ar detectors are used.

The $UM\alpha$ - $UM\beta$ region of high-Th-content standards [e.g., ThO_2 , $ThSiO_4$, $CaTh(PO_4)_2$] presents several analytical

TABLE 3. Spectral interferences in chemical dating of monazite

wavelength (Å)	L (mm) ($R_R=140$ mm)	line	Peak or background	order
Part I: $PbM\alpha$ (5.286 Å/169.307 mm for $R_R=140$ mm)				
5.372	172.061	$SK\alpha_1$	background	1
5.340	171.036	$ThM\zeta_2$	peak	1
5.331	170.748	$LaL\alpha_1$	peak	2
5.283	169.211	$YL\gamma_{2,3}$	peak	1
5.245	167.994	$ThM\zeta_1$	peak	1
5.236	167.705	$ThM2-O4$	peak	2
5.123	164.086	$CeL\alpha_1$	background	2
5.076	162.581	$PbM\beta$	background	1
5.050	161.748	$UM\zeta_2$	background	1
5.032	161.559	$SK\beta_1$	background	1
4.946	158.417	$UM\zeta_1$	background	1
4.918	157.520	$LaL\beta_1$	background	2
4.899	156.911	$LaL\beta_3$	background	2
4.821	154.413	$LaL\beta_3$	background	2
4.741	151.851	$NdL\alpha_1$	background	2
4.712	150.922	$CeL\beta_1$	background	2
4.699	150.506	$CeL\beta_4$	background	2
4.622	148.039	$CeL\beta_3$	background	2
4.606	147.527	$LaL\beta_{2,15}$	background	2
Part II: $UM\beta$ (3.716 Å/119.021 mm for $R_R=140$ mm)				
4.072	130.023	$NdL\beta_{2,15}$	background	2
3.941	126.227	$ThM\beta$	background	1
3.910	125.234	$UM\alpha_1$	background	1
3.871	123.985	ArK abs edge	background	1
3.808	121.967	$ThM4-O2$	background	1
3.760	120.430	$ThM5-P3$	peak	1
3.756	120.302	$NdL\gamma_1$	peak	2
3.741	119.822	$KK\alpha_1$	peak	1
3.729	119.437	$ThM5$ abs edge	peak	1
3.718	119.085	$ThM3-N4$	peak	1
3.679	117.836	$ThM\gamma$	peak	1
3.603	115.401	$NdL\gamma_2$	background	2
3.568	114.284	$ErL\alpha_1$	background	2
3.557	113.928	$ThM4$ abs edge	background	1
3.479	111.430	$UM\gamma$	background	1
3.454	110.626	$KK\beta_{1,2}$	background	1
3.362	107.671	$CaK\alpha_2$	background	1
3.358	107.567	$CaK\alpha_1$	background	1

difficulties due to the combination of numerous ThM lines, plus background discontinuities generated by $ThM5$ and $M4$ absorption edges (Fig. 8b). $UM\alpha$ is overlapped by $ThM\beta$, and $UM\beta$ is overlapped by a combination of $ThM\gamma$, $ThM3-N4$, and $ThM5-P3$. Potential $UM\beta$ backgrounds are subject to $ThM4-O2$, $M4-P2$, and $M2-N1$ interference. Theoretical and empirical interference corrections for Th overlaps of both $UM\alpha$ and $M\beta$ (Pyle et al. 2002) show that correction for $ThM\beta$ interference is approximately twice as large as the combined correction for $ThM\gamma$, $M3-N4$, and $M5-P3$.

Collection of background intensity in high-Th standards (and unknowns) is hampered by the above Th line interferences, $ThM5$ and $M4$ absorption edges, and, for 1-atm Ar detectors, the Ar K-absorption edge as well. In high-Th samples, the proximity of the $M5$ and $M4$ absorption edges makes 2-point-linear or 2-region-exponential background interpolation problematic. Collection of background between $ThM5-P3$ and $M4-O2$ (high) and between $ThM4-P2$ and $ThM\gamma$ (low) results in a Th-U correction factor, as measured on $ThSiO_4$, that is $\sim 20\%$ lower than one with background intensities measured between $ThM4-O2$ and the Ar K-absorption edge (high) and between $ThM2-N1$ and $ThM4-P2$ (low). Jercinovic and Williams (2005) indicated that $ThM5$ and $M4$ absorption edges are definable, for 1σ background measure-

TABLE 4. Calculated intensities for 2-point and exponential background fits to monazite WD spectra from Trebilcock and T22

	PbM α				UM β			
	Trebilcock (Fig. 10)		T22 (Fig. 11)		Trebilcock (Fig. 13)		T22 (Fig. 14)	
	Ar	Xe	Ar	Xe	Ar	Xe	Ar	Xe
Peak position	170.85	170.75	170.75	170.8	120.5	120.55	120.45	120.6
I_p	0.4052	0.3410	0.2805	0.2305	1.9788	1.4150	1.4492	0.9328
2-pt high 1 offset	6.15	6.25	6.30	6.25	2.00	2.00	2.00	2.50
Exp 1 high interval	4.15–8.15	4.25–8.25	4.30–8.30	4.25–8.25	1.50–2.50	1.50–2.50	1.50–2.50	1.40–3.40
2-pt low 1 offset	3.75	3.90	3.45	3.90	4.00	4.00	2.55	3.60
Exp 1 low interval	4.25–3.25	4.75–3.05	3.95–2.95	4.80–3.10	5.00–3.00	5.00–3.00	2.95–2.15	4.60–2.60
2-pt high 2 offset	6.15	6.25	6.30	6.25	–	–	2.00	–
Exp 2 high interval	4.15–8.15	4.25–8.25	4.30–8.30	4.25–8.25	–	–	1.50–2.50	–
2-pt low 2 offset	9.05	8.95	9.25	9.30	–	–	3.50	–
Exp 2 low interval	9.85–8.25	9.75–8.15	9.75–8.75	9.80–8.80	–	–	3.65–3.35	–
$I_{B(2p1)}$	0.2650	0.2130	0.2360	0.1832	1.1470	0.7935	1.0168	0.6440
$I_{B(exp1)}$	0.2632	0.2108	0.2345	0.1820	1.1450	0.7932	1.0152	0.6440
$I_{B(2p2)}$	0.2588	0.2108	0.2320	0.1862	–	–	1.0082	–
$I_{B(exp2)}$	0.2568	0.2065	0.2305	0.1822	–	–	1.0062	–
$I_{P-B(2p1)}$	0.1403	0.1279	0.0446	0.0474	0.8318	0.6216	0.4324	0.2886
$I_{P-B(exp1)}$	0.1419	0.1303	0.0460	0.0486	0.8337	0.6216	0.4340	0.2888
$I_{P-B(2p2)}$	0.1465	0.1301	0.0484	0.0444	–	–	0.4410	–
$I_{P-B(exp2)}$	0.1485	0.1345	0.0501	0.0483	–	–	0.4429	–

Notes: Peak positions in mm; PET diffraction crystal ($2d = 8.74 \text{ \AA}$), 140 mm Rowland Circle. Peak (I_p) and Peak minus Background (I_{p-B}) intensities in counts/nA*s. Scan parameters: 200 nA cup current, 0.5 mm/step, 20 s/step. Offsets and intervals in mm, relative to peak position. 2p = two point background fit, exp = exponential background fit; "1" and "2" refer to fits with high background point/intervals no. 1 and no. 2, respectively (see text).

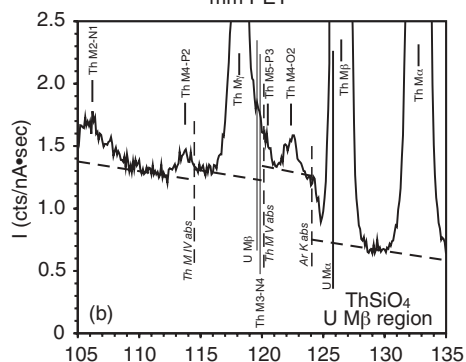
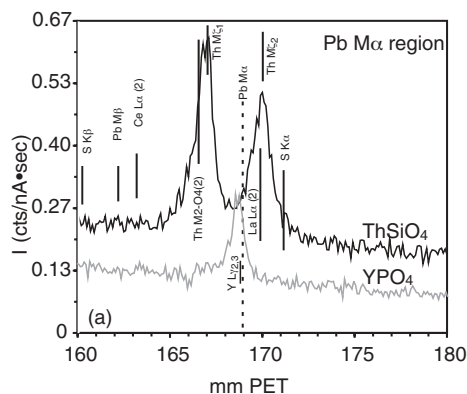


FIGURE 7. PbM α and UM β interferents. (a) WD intensity scans of ThSiO $_4$ and YPO $_4$ in the region of PbM α , showing positions of interfering peaks ThM ζ_1 , ThM ζ_2 , and YL $\gamma_{2,3}$ relative to PbM α . Also shown on the scan are theoretical positions of potentially interfering lines such as SK α , LaL α , CeL α , PbM β , and SK β . The (2) adjacent to La and Ce labels indicates the line is a second-order reflection. (b) WD intensity scan of ThSiO $_4$ in the region of the UM β peak. UM β and Th M-series peak positions indicated by solid vertical lines; ArK and ThM5 and M4 absorption edges indicated by dashed vertical lines. The approximate intensity of the bremsstrahlung between Th M2-N1 and ThM α , with discontinuities at the absorption edges, is indicated by the sub-horizontal dashed lines.

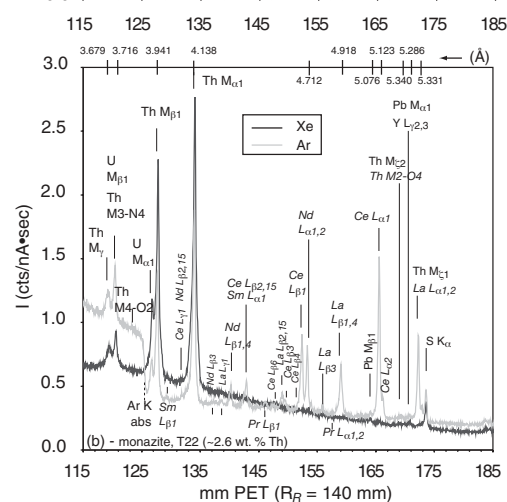
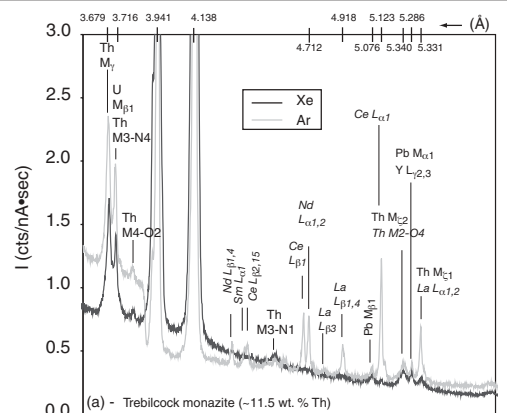


FIGURE 8. WD intensity scans of (a) Trebilcock monazite (Tomascak et al. 1996) and (b) monazite T22 (Spear et al., in revision) over the region 3.6–5.6 \AA . Scans using a 1-atm Ar detector are shown in gray, and scans using a sealed Xe detector are shown in black. Discernable peaks are labeled using Siegbahn (1931) notation where applicable, or shell-transition notation if no Siegbahn notation exists. Scan parameters include 15 keV accelerating voltage, 200 nA cup current, 20 μm beam diameter, 0.05 mm spectrometer step increment, and 20 s dwell/step.

ment precisions of 0.5%, at approximately 4 wt% Th and 8 wt% Th, respectively. The most accurate assessment of background intensity at the $UM\beta$ position in high-Th standards involves scans of the region between $ThM4-P2$ and $ThM\gamma$.

Xe and 1 atm Ar WD spectra—unknowns

Four WD spectra from two monazite grains are depicted in Figure 8. Trebilcock (Fig. 8a) is a high-Th (11–14 wt%) monazite from granitic pegmatite of the Trebilcock quarry in Topsham, ME (Tomascak et al. 1996). Sample T22 is from the Cavendish Formation (Star Hill, VT) on the northeastern Flank of the Chester Dome (Fig. 8b; Spear et al. in revision). It contains monazite with low-Th cores (~2.5 wt%) and high-(U, Th) overgrowths; the scan shown in Figure 8b is from the core of a monazite included in garnet.

The WD spectra in Figure 8 encompass the region containing the $M\alpha$ and $M\beta$ lines of Pb, Th, and U. Gas-flow Ar detector scans are shown in gray, and sealed Xe detector scans are shown in black. The effect of detector gas on monazite WD spectra is demonstrated in these two plots. The energy differential between Ar and second-order LREE X-rays results in LREE escape peaks that are unfilterable with differential PHA if the detector is optimized for Pb analysis. The energy differential between second-order LREE and Xe X-rays permits filtering of LREE escape peaks with differential PHA. Several first-order lines are visible in the WD spectra. Second-order LREE lines, however, are greatly diminished in intensity relative to the same lines in the 1-atm Ar detector.

Although the counting rates for Pb are higher on the 733 for the 1-atm Ar detector relative to the Xe detector, the potential peak and background interferences due to second-order LREE X-ray lines—along with interferences from first-order X-ray lines (Fig. 8; Table 3)—compromise the usefulness of the 733’s 140 mm R_R , 1-atm Ar X-ray detectors for precise Pb analysis. The 733’s Xe detectors produce spectra free from detector gas absorption edge and second-order LREE interferences in the regions of analytical interest surrounding the $M\alpha$ and $M\beta$ lines of both lead and uranium.

The WD spectra shown in Figure 8 are representative of the most common compositional variation in monazite; namely, the LREE-Th exchange (either as brabantite or huttonite). As the huttonite or brabantite component increases, Th line overlaps on $PbM\alpha$ and $UM\beta$ become more severe, as do the magnitudes of the $ThM4$ and $M5$ absorption edges in the vicinity of $UM\beta$. As the $LREEPO_4$ component increases, Th line overlaps decrease in severity, but interferences caused by lower intensity LREE peaks (e.g., $L\beta$, $L\gamma$) become more problematic for 1-atm Ar detectors.

Pb region of interest

The Pb analytical region for both Trebilcock and T22 monazite is shown in expanded view in Figure 9. High-detail scans of the Pb region of interest are necessary for selection of points or regions for background collection. The scans shown here were collected at 200 nA, with a step size of 0.05 mm and a dwell time of 20 s/step.

The P-B value for the Trebilcock $CeL\alpha_1$ line is approximately 40 times greater on the Ar detector (0.95 cts/nA·s vs. 0.025 cts/

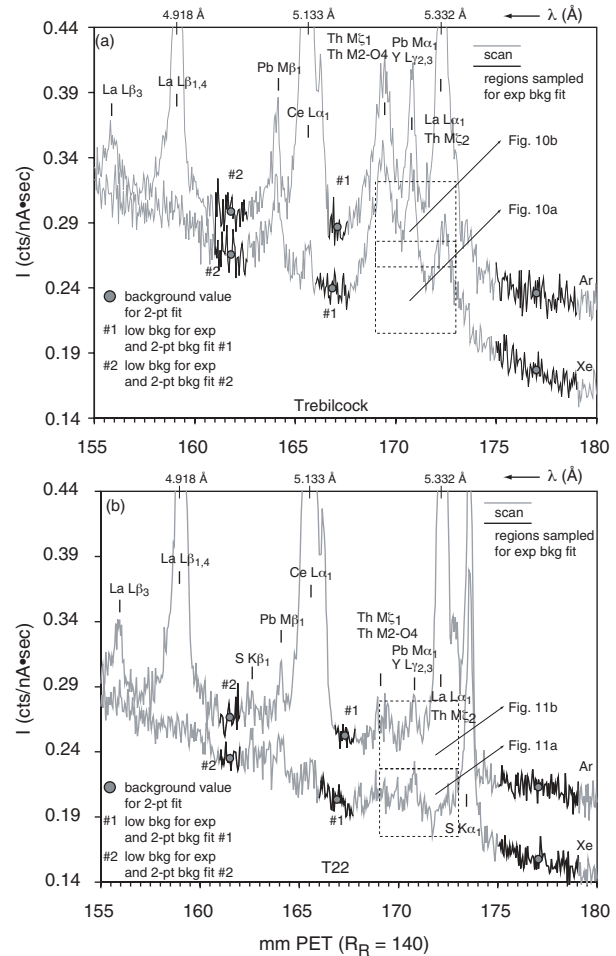


FIGURE 9. Detailed WD intensity scan of the $PbM\alpha$ peak and background region for (a) Trebilcock monazite and (b) monazite T22. Each panel contains a 1-atm Ar detector scan (higher intensity spectra) and a sealed Xe detector scans (lower intensity spectra). Resolvable X-ray lines are indicated with solid vertical lines and corresponding notation. Spectral regions sampled for background fits are shown in black. Where two low-background regions are shown, background intensity at the $PbM\alpha$ position is calculated for both sets of low backgrounds (e.g., bkg 1, bkg 2). Background intensities for linear extrapolation (gray circles) are calculated by linear regression for each background region and use the regressed intensity value at the mid-point of that region. Locations of Figures 10a (Xe scan), 10b (Ar scan), 11a (Xe scan), and 11b (Ar scan) are indicated by the dashed boxes. Scan parameters are identical to those given in Figure 8.

nA·s), and the same line in T22 is approximately 50 times more intense than when measured with a Xe detector (1.50 cts/nA·s vs. 0.031 cts/nA·s). Intensities of the La lines ($L\alpha_1$, $L\beta_{1,4}$, $L\beta_3$) are correspondingly lower, as well, on the Xe scans. The significant differences between the scans of Trebilcock and T22, regardless of detector, are: (1) the apparent intensities of the Pb peaks, and (2) the intensities of the $ThM\zeta_1$ and $M\zeta_2$ peaks. The apparent intensity of the $PbM\alpha$ peak includes contributions from the $ThM\zeta$ peaks as well as $YL\gamma_{2,3}$; Trebilcock is Y-rich in comparison to T22 (~1.8 us. 0–0.3 wt% Y_2O_3).

In each scan, an interference-free region of the continuum

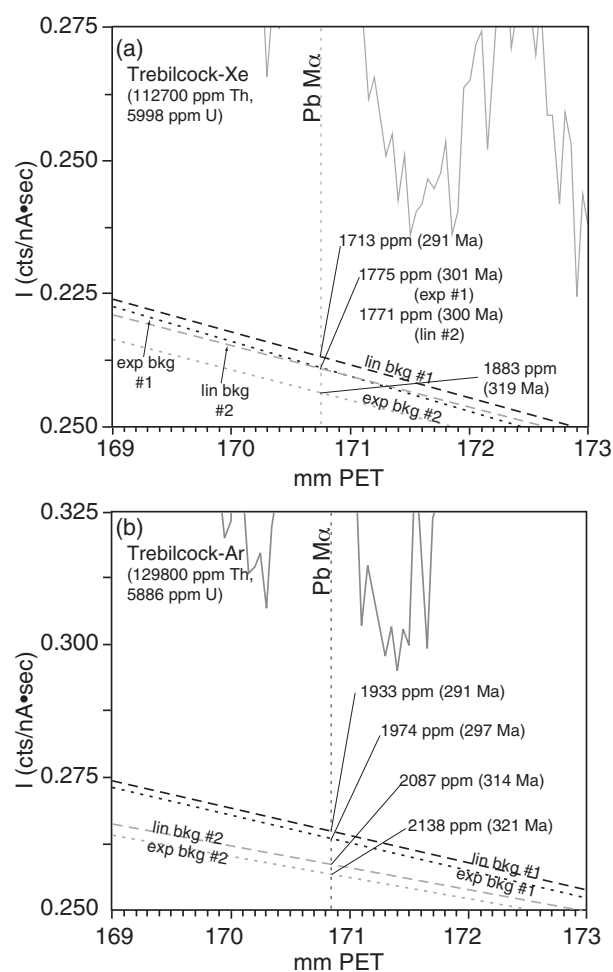


FIGURE 10. Interpolated background intensities at the $PbM\alpha$ peak position, Trebilcock monazite, for both (a) Xe and (b) Ar detectors. The $PbM\alpha$ position is indicated by the vertical dashed line. The version and type of background extrapolation used (linear 1, exponential 1, linear 2, etc.) is indicated on the fit line. ZAF-corrected Pb concentration (using measured U and Th concentrations indicated on the figure) and age are given for each background fit. Interpolated background intensities are given in Table 5. For Figures 10, 11, 13, and 14, the symbolism used for the background extrapolations is as follows: long dashed black line = linear fit, background pair 1; short dashed black line = exponential fit, background pair 1; long dashed gray line = linear fit, background pair 2; short dashed gray line = exponential fit, background pair 2.

is selected (black line segments) for calculation of background intensity at the $PbM\alpha$ position. Two high-background regions are selected for comparison (Table 4). High background 1 is sampled between $ThM\zeta_1$ and $CeL\alpha_1$, and high background 2 between $PbM\beta$ and $LaL\beta_{1,4}$. For each pair of backgrounds, $PbM\alpha$ net intensity (P-B cts/nA·s) is calculated using both a 2-point linear interpolation and an exponential fit. Each of the intensity values for the 2-point (linear) interpolation of background intensity at the peak position is obtained from a linear regression over the length of the sampling interval, taking the regression value at the mid-point of the interval. Calculation of Pb concentration is referenced to quantitative analyses using two-point backgrounds

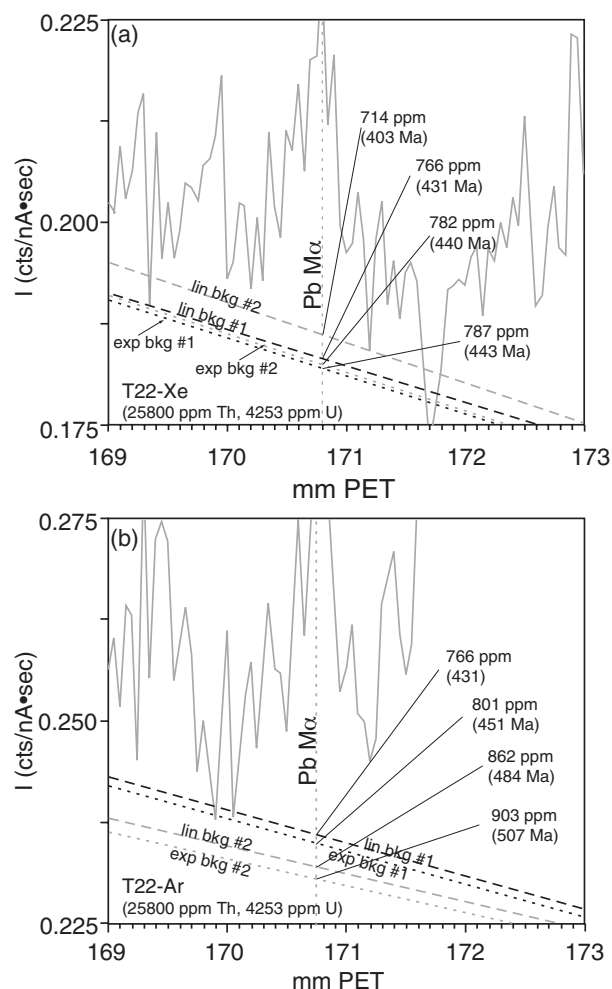


FIGURE 11. Interpolated background intensities at $PbM\alpha$ peak position, monazite T22, for both (a) Xe detector and (b) 1-atm Ar detector. Symbolism identical to that used in Figure 10. Measured Th and U concentrations used to calculate ages given on the figure.

collected at the low and high 1 background positions. The results of the four background fits are shown in Table 4, Figure 10 (Trebilcock) and Figure 11 (T22).

An interference-corrected Pb concentration of 1713 ppm for Trebilcock was measured using a Xe detector, $PbM\alpha$ and the 2-point linear background 1 (Table 4). The scan in Figure 10a shows a net $PbM\alpha$ intensity of 0.1279 cts/nA·s for this background selection. Assuming that the ZAF corrections are identical for a given sample and detector, a lower background intensity simply scales to an additive amount of Pb. The lowest Pb concentration and youngest date (for measured Th and U concentrations shown in Fig. 10a) is given by linear background 1 (1713 ppm, 291 Ma). Exponential background 1 and linear background 2 give nearly identical Pb concentrations and dates (1775 ppm, 301 Ma, and 1771 ppm, 300 Ma, respectively). Exponential background 2 yields the highest Pb concentration and oldest date (1883 ppm, 319 Ma), which is roughly 10% greater than linear background 1, a percentage approximately equal to the 2σ counting statistics for Pb in this monazite. The dates are calculated using fixed Th

and U concentrations (Fig. 10a).

An independent analysis of Trebilcock Pb concentration using the 1-atm Ar detector paired with linear background 1 yields an interference-corrected concentration of 1933 ppm (291 Ma) in a region of slightly higher Th and lower U concentration (Fig. 10b). The results of the four background fits are similar, with an total increase in calculated Pb concentration from linear background 1 to exponential background 2 (2138 ppm, 321 Ma) of 11%, and a correspondingly older date (Fig. 10b).

Two points are emphasized by the different background fits: (1) barring interference, an exponential fit always yields a lower background value than the corresponding linear interpolation, and this difference in calculated background increases with increasing 2-point separation (increasing $\Delta\lambda$); (2) for high-Th samples (e.g., Trebilcock), placement of the $PbM\alpha$ low background between $ThM\zeta_1$ and $PbM\beta$ may result in lower apparent Pb concentration, and younger apparent age, due to $ThM\zeta_1$ interference on the low $PbM\alpha$ background.

For sample T22, Pb concentrations from the different background fits are referenced to a measured Pb concentration of 766 ppm (2 point background, high background 1, Xe detector). Linear background 2 on the Xe detector (Fig. 11a) gives a high background, and consequently low Pb concentration (714 ppm) relative to linear background 1 and exponential backgrounds 1 and 2. The high-background value from linear 1 may be due to a slightly broader $SK\beta$ peak on the Xe scan (Fig. 11a). For the Ar scan (Fig. 11b), background decreases (and P-B increases) from linear 1 to exponential 2. The range in calculated Pb concentration is 73 ppm (10% relative) on the Xe detector, and 137 ppm (18% relative) on the Ar detector. For measured Th and U concentrations given in Figure 11, dates range from 403 to 443 Ma (Xe detector, Fig. 11a) and 431 to 507 Ma (Ar detector, Fig. 11b).

Because of its additive nature, seemingly small changes in background intensity at the $PbM\alpha$ position are capable of producing statistically significant changes in apparent Pb concentration, especially as true Pb concentration decreases. Overestimation of background in high-Th monazite can be mitigated by collection of background between $PbM\beta$ and $LaL\beta_{1,4}$, but the $SK\beta$ region must be avoided if S is present in the monazite, or overestimation of background intensity will result.

Monazite spectral complexity in the Pb region of interest, coupled with low Pb concentrations, make permanent assignment of Pb background positions risky. If two-point backgrounds are to be used, examination of WD scans and background fits will aid in elimination of potential inaccuracies in background collection.

U region of interest

In a Th-rich monazite such as Trebilcock, the severity of the $UM\alpha$ - $ThM\beta$ and $UM\beta$ - $ThM\gamma$ overlaps (Fig. 12a) is apparent. At these Th concentrations, $ThM5-P3$ and $M4-O2$ peaks are also resolvable. In monazite T22 (Fig. 12b), lower Th concentration results in less severe $UM\alpha$ - $ThM\beta$ and $UM\beta$ - $ThM\gamma$ overlaps. Consequently, second-order LREE peaks $ErL\alpha_{1,2}$, $NdL\gamma_2$ are resolvable; the top of the $NdL\gamma_1$ peak may be discernable between $ThM\gamma$ and $UM\beta$. At wavelengths shorter than the Ar K-absorption edge, the continuum is noticeably more curved on the Ar scans

than the Xe scans.

The results of background fits in the U ROI are shown in Figures 13 and 14. One pair of backgrounds was used on Trebilcock and the Xe-detector T22 scan. Two sets of low backgrounds were selected on the T22 Ar-detector scan; one between $ThM\gamma$ and $NdL\gamma_2$, and one between $NdL\gamma_2$ and $ErL\alpha_{1,2}$. For Trebilcock, the calculated U concentrations are referenced to a measured concentration of 5887 ppm U (PETJ crystal, 1-atm Ar detector) with a two-point background interpolation. For T22, the calculated U concentrations are referenced to a measured concentration of 4253 ppm U (PETJ crystal, 1-atm Ar detector) with a two-point background interpolation (low background 1).

Calculated U concentrations in Trebilcock using a 2-point vs. exponential background fit are statistically indistinguishable ($\sigma_U = 2.5\%$) for both Xe (Fig. 13a) and Ar (Fig. 13b) detectors. In

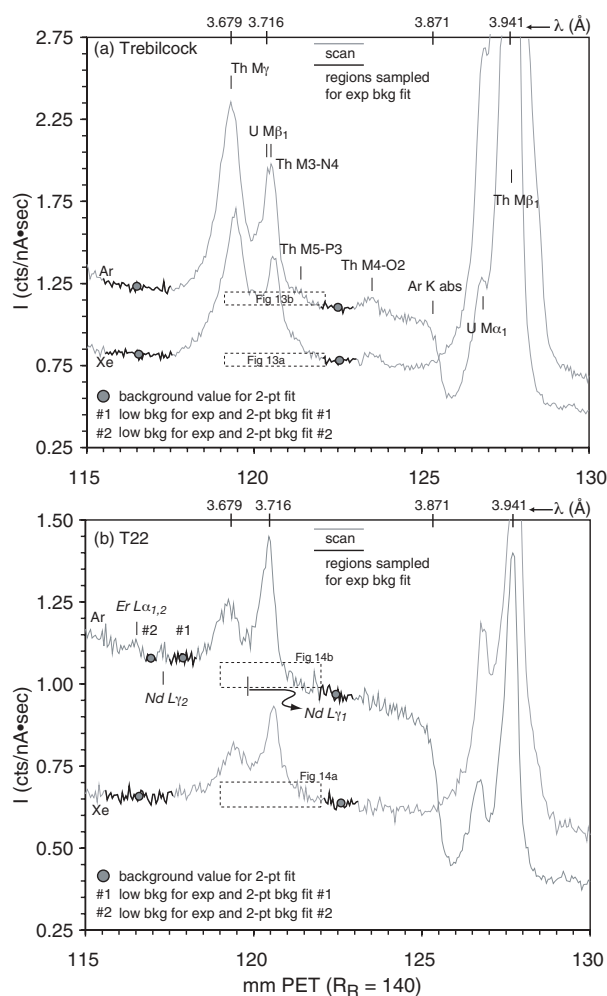


FIGURE 12. Detailed WD intensity scan of the $UM\beta$ peak and background region for (a) Trebilcock monazite and (b) monazite T22. Each panel contains a 1-atm Ar detector scan and a sealed Xe detector scan indicated by “Ar” and “Xe,” respectively. Spectral regions sampled for background fits are shown in black. Symbolism is identical to that used in Figure 9. Locations of Figures 13a (Xe scan), 13b (Ar scan), 14a (Xe scan), and 14b (Ar scan) are indicated by dashed boxes. Scan parameters are identical to those given in Figure 8. Measured Th and Pb concentrations used to calculate ages are given on the figure.

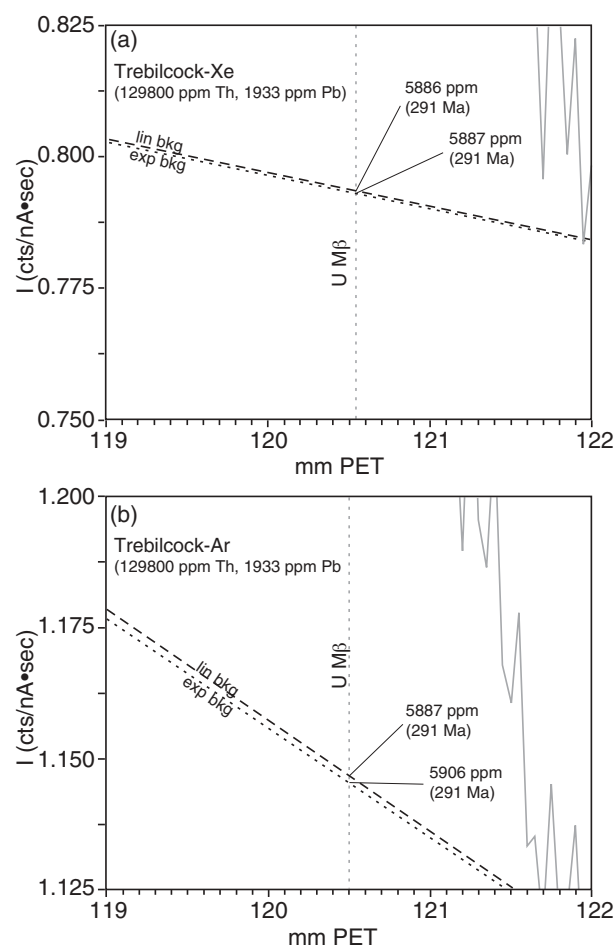


FIGURE 13. Interpolated background intensities at the $UM\beta$ peak position, Trebilcock monazite, for both (a) Xe detector and (b) 1-atm Ar detector. Symbolism identical to that used in Figure 10. Measured Th and Pb concentrations used to calculate ages are given on the figure.

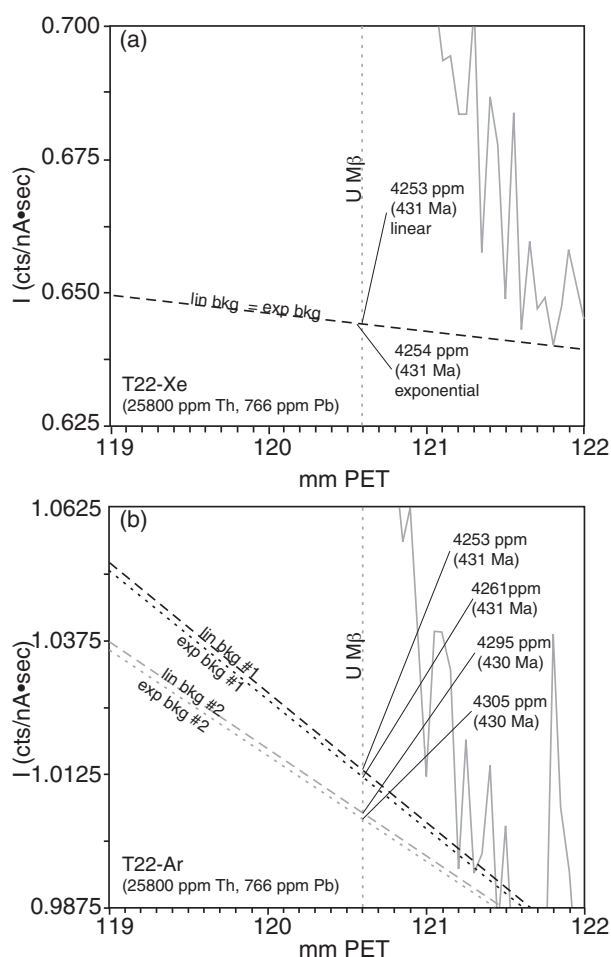


FIGURE 14. Interpolated background intensities at the $UM\beta$ peak position, monazite T22, for both (a) Xe detector and (b) 1-atm Ar detector. Symbolism is identical to that used in Figure 10. Measured Th and Pb concentrations used to calculate ages are given on the figure.

T22, 2-point and exponential background fits produce identical background intensities and calculated U concentrations for scans using a Xe detector (Fig. 14a). For 1-atm Ar scans of T22 (Fig. 14b), linear and exponential fits to the same background pair are not distinguishable at the uncertainty of the T22 U analysis ($\sigma_U = 2.5\%$). Background intensities at the $UM\beta$ position using low background 2 are slightly lower than intensities calculated with low background 1 (Table 4), but generate concentrations that are not statistically resolvable at the precision of the U analysis.

Variation in the $UM\beta$ background fits for both Trebilcock and T22 generate no change in the calculated dates (Figs. 13 and 14). For these two samples, microprobe ages are less sensitive to variations in the modeling of background intensity for $UM\beta$ than for $PbM\alpha$. However, the measured U concentration, regardless of the background calculation method, is still subject to error arising from uncertainty in the true background intensity at $UM\beta$ due to the presence of the $ThM5$ and $M4$ absorption edges, and this error increases as U concentration decreases. For high-Th samples (Jercinovic and Williams 2005), this error can be significant, and detailed scans of the $UM\beta$ region should be undertaken

to: (1) assure that the $UM\beta$ low background is free from $ThM\gamma$ interference, and (2) account for the effect of the $ThM5$ and $M4$ absorption edges to the most accurate extent possible.

ANALYTICAL PRECISION IN MICROPROBE DATING OF MONAZITE

Poisson statistics

After selection of analytical line, background collection region(s), background fitting method, and interference correction method for Th, U, and Pb, analyses must be examined for single-spot precision. Analytical precision, modified for interference, statistics of genetically related groups, and systematic errors, will determine the overall precision of microprobe dates used to make paragenetic or tectonic interpretations.

For the purposes of discussion, it is assumed that the precision of a monazite microprobe date is solely a function of the counting (Poisson) statistics of the elemental concentrations measured during analysis. Systematic errors arising from EMPA configuration, data reduction, inherent monazite properties, or some combination thereof, are addressed in the section

on analytical accuracy.

The basics of Poisson statistics, and formulas for absolute and relative analytical standard deviation, as applied to EMPA, are presented by Scott et al. (1995). The standard deviation of the *k*-ratio ($\sigma_{P-B,k\text{-ratio}}$) is found by applying the simplified formula (all covariance terms equal to zero) for the standard deviation of a ratio *a/b* (Bevington 1969); *a*, in this case, is the formula for the standard deviation of P-B counts on the unknown, and *b* is the formula for the standard deviation of the P-B counts on the standard. Partial differentiation of *a/b* with respect to *a* and *b* yields:

$$\sigma_{P-B,k\text{-ratio}}^2 = \left[\frac{1}{2 \left(\frac{N_{P,unk}}{t_{P,unk}^2 \text{curr}_{P,unk}^2} + \frac{N_{B,unk}}{t_{B,unk}^2 \text{curr}_{B,unk}^2} \right)^{1/2} \left(\frac{N_{P,std}}{t_{P,std}^2 \text{curr}_{P,std}^2} + \frac{N_{B,std}}{t_{B,std}^2 \text{curr}_{B,std}^2} \right)^{1/2}} \right]^2 \sigma_{P-B,unk}^2 + \frac{1}{2} \cdot \left[\frac{\left(\frac{N_{P,unk}}{t_{P,unk}^2 \text{curr}_{P,unk}^2} + \frac{N_{B,unk}}{t_{B,unk}^2 \text{curr}_{B,unk}^2} \right)^{1/2}}{\left(\frac{N_{P,std}}{t_{P,std}^2 \text{curr}_{P,std}^2} + \frac{N_{B,std}}{t_{B,std}^2 \text{curr}_{B,std}^2} \right)^{3/2}} \right]^2 \sigma_{P-B,std}^2 \quad (3a)$$

where $N_{P,unk(std)}$ and $N_{B,unk(std)}$ equal counts per nA·s of peak and background on the unknown (standard). The relative standard deviation of peak minus background counts on the *k*-ratio is given by

$$\epsilon_{P-B,k\text{-ratio}} = \sqrt{\epsilon_{P-B,std}^2 + \epsilon_{P-B,unk}^2} \quad (3b)$$

Calculation of the statistic in Equation 3b is simpler, and the relative standard deviation is a more useful value, as it relates directly to the uncertainty in the age calculation for a single analysis. Assuming that X-ray production scales linearly with current, count accumulation to the desired precision is achieved by maintaining a constant current-time (nA·s) product.

With the exception of Proterozoic or older, U-poor monazite (e.g., Daniel and Pyle 2002), the limiting factor in monazite age

analysis is the precision associated with measurement of Pb. Thus, optimizing Pb analysis for maximum precision will, in most cases, result in the most precise age determination. However, the precisions associated with the analyses of elements that interfere with Pb also have a direct bearing on the final precision of the Pb analysis (see below).

Current and counting time

For the JEOL 733 Superprobe at RPI, an intrinsic detector response of ~0.33 counts Pb/s·nA·wt% Pb is measured at 25 keV and 200 nA with a PET crystal and a Xe detector. Figure 15 shows Pb analytical precision for this detector response, and a measured detector response of 0.11 counts/s·nA at high and low background positions. For Pb concentrations of 10000 ppm, 1500 ppm, and 250 ppm, 10 minutes of counting on both peak and background (dashed line, Fig. 15b) results in 1σ counting errors of 0.5, 2, and 12% for the 10000 ppm Pb, 1500 ppm Pb, and 250 ppm Pb monazites, respectively. These uncertainties translate to 2σ compositional uncertainties of ±92 ppm Pb, ±62 ppm Pb, and ±58 ppm Pb, respectively.

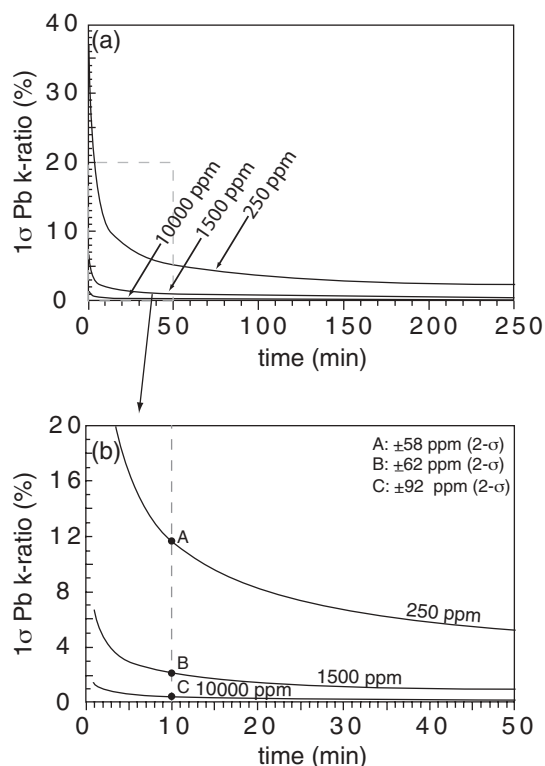


FIGURE 15. Plot of Pb counting error vs. time. An intrinsic detector response of 0.33 counts Pb/s·nA·wt% Pb, measured at 200 nA on Trebilcock monazite, was used to construct this figure. (a) Plot of Pb 1σ counting error vs. time for material with 10000 ppm Pb (bottom line), 1500 ppm Pb (middle line), and 250 ppm Pb (top line). Boxed area in a is expanded in (b), showing detail of counting precision with changing time, up to a maximum of 50 minutes. One-sigma counting errors at 10 minutes are 11.7% (point A), 2.1% (point B), and 0.5% (point C) for 250, 1500, and 10000 ppm Pb, respectively. The quoted counting errors translate to 2σ compositional uncertainties shown in b.

Interference corrections and precision

As measured on the 733, $PbM\alpha$ is approximately 30% more intense than $PbM\beta$, and analysis of the $PbM\alpha$ line is correspondingly more precise. However, the true precision of the $PbM\alpha$ analysis is less than that of the raw k -ratio, due to interference from Th and Y X-ray lines. The corrected $PbM\alpha$ analytical precision decreases because: (1) some number of $PbM\alpha$ counts are, in reality, $ThM\zeta_{1,2}$ and $YL\gamma_{2,3}$ counts; and (2) the Pb interference correction is a function of Th and Y concentration, each of which carries an inherent analytical uncertainty. It is therefore a useful exercise to determine, by error propagation, how much additional error is added to $PbM\alpha$ analytical precision by interference corrections.

Interference correction methods and the full error propagation for the uncertainties in interference-corrected $PbM\alpha$ and $UM\beta$ analyses are presented in Appendix 1. In summary, the corrections for Th and Y interference on Pb introduce a trivially small amount of additional uncertainty to the analysis. The additional error is a function of: (1) age (i.e., Pb content), and (2) concentration of interfering elements. For ~1400 Ma monazite from northern New Mexico (Pyle and Daniel, in prep), error in corrected relative standard deviation (RSD) for $PbM\alpha$ is on the order of 0.000001 to 0.0001% greater than the uncorrected RSD,

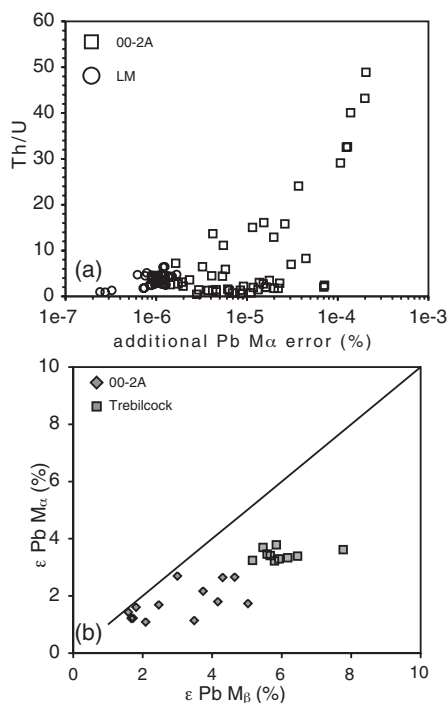


FIGURE 16. (a) Plot of monazite Th/U ratio vs. additional $PbM\alpha$ counting error introduced by correcting for $ThM\zeta_1$, $ThM\zeta_2$, and $YL\gamma_{2,3}$ interferences. Details of error propagation are given in Appendix 1. Squares = monazites, sample 00-2A (Daniel and Pyle 2002; Pyle and Daniel, unpublished); circles = monazites, LM samples (Pyle and Spear 2004). (b) Plot of counting error for replicate lead measurements using $PbM\beta$ and $PbM\alpha$. Squares = Trebilcock monazite; diamonds = monazites, sample 00-2A.

and is a strong function of monazite Th content (Fig. 16a). An ~380 Ma monazite from central New England (Pyle and Spear 2004) has a restricted Th/U ratio, and has corrected $PbM\alpha$ RSD that is generally 0.000001% greater than the uncorrected RSD. In general, as long as Th and Y standards are compositionally well-characterized (for purposes of interference correction), $PbM\alpha$ should be the analytical line of choice.

Replicate analyses of the same monazite spot using both $PbM\alpha$ and $PbM\beta$ (Fig. 16b) show the increased precision associated with $PbM\alpha$ analysis for Trebilcock monazite and monazite (sample 00-2A) from the mid-Proterozoic of northern New Mexico. Precision for $PbM\beta$ approaches precision for $PbM\alpha$ as Pb concentration increases, but for Trebilcock monazite (~1800 ppm Pb), $PbM\alpha$ is 2–4% more precise than $PbM\beta$.

Age precision of monazite populations

If monazite analyses are drawn from a single age population, it is expected that the mean sample age approximates the true monazite age, and the variation of the age estimates about the mean, disregarding correlations in U, Th, and Pb errors, is described by the quadratic sum of U, Th, and Pb analytical uncertainties. If the ages are normally distributed about the mean, approximately 95% of the age determinations will be within $\pm 2\sigma$ of the mean age.

However, multiple domains may be recognized within a single monazite grain, and separated on a compositional or textural (i.e., age-independent) basis. If distinct monazite domains recur systematically in a sample or related group of samples, these domains may be correlated with specific monazite-forming reactions (Pyle and Spear 2003), deformation events (Williams and Jercinovic 2002), or fluid infiltration (Harlov and Förster 2003). Multiple age domains (Wendt and Carl 1991; Montel et al. 1996; Cocherie and Albarede 2001) also may be uncovered by microprobe dating, provided that the mean ages of two or more monazite populations are statistically distinguishable at the level of analytical precision associated with the “average” single-spot analysis in all domains.

Each point analysis within an independently defined domain represents a sample “date” from the domain population. The age of each domain is described by the weighted average of the “dates” of all points sampled within the domain, and the precision to which the domain age is known is described by the standard error of the mean domain age. For n sampled points x_i in each population (domain), the weighted mean domain age \bar{x} , and associated standard error of the mean (se) are given by (Bevington 1969):

$$\bar{x} = \frac{\sum_{i=1}^n x_i}{\sum_{i=1}^n \frac{1}{\sigma_i^2}} \quad (4a)$$

$$se = \left(\frac{1}{\sum_{i=1}^n \sigma_i^2} \right)^{\frac{1}{2}} \quad (4b)$$

Thus, as the sample size (i.e., number of “dates”) in each

domain increases, so does the precision of the domain age estimate.

With regard to geochronology, perhaps the greatest utility of the EMPA lies in combining in-situ textural and compositional data, revealed by back-scattered electron imaging and element-distribution mapping, and age determinations. Monazite domains are commonly classified by systematic, well-defined compositional breaks. Pyle and Spear (2003) investigated low-pressure migmatites from SW New Hampshire, and correlated 4 such monazite compositional domains with major phase reactions. The results of the EMPA age analysis of these monazites, plus weighted average domain ages and associated standard errors are presented in a companion paper included in this volume (Pyle and Spear 2005).

ACCURACY OF MONAZITE MICROPROBE AGES

Components of accuracy

Statistical precision is one component of the total error involved in monazite microprobe dating. The sum of random and systematic errors gives an estimate of the accuracy of the age, provided that the true age of the grain in question is known a priori. If it is assumed that analytical uncertainty is the sole source of random error, then the residue of inaccuracy resides in systematic errors associated with monazite microprobe dating. These systematic errors may be classified as instrumental errors, operator errors, and specimen errors. All of these errors are, to some degree, quantifiable. Furthermore, the sign of these errors may be unidirectional positive, unidirectional negative, or the error values may fluctuate about a mean value. Thus, an age estimate may be “accurate,” but only due to cancellation of multiple errors. Several systematic errors, and associated magnitudes, are listed in Table 5.

Instrumental errors

Instrumental errors include, but are not limited to (1) instability of and errors in measuring accelerating voltage and beam

current; (2) changes in diffraction crystal interplanar spacing; (3) instability of gas-amplification of proportional counter; (4) dead-time losses in X-ray detector and electronic counting circuitry; and (5) shift and distortion of pulse-height distributions. Discussions that follow are specific to the JEOL 733, but such errors may occur in any EMPA.

Dead time and current measurement. Although separate issues, the effects of improper calculation of deadtime and errors in current measurement (non-linearity) may be difficult to decouple as they are manifested in measured U, Th, and Pb concentrations. The 733 at RPI uses a self-contained pulse-processing system (Geller and Herrington 2002) to reject voltage pulses that are received in a time interval less than that needed to shape and amplify a single pulse. Counter dead time is calculated and updated digitally, rather than imposed via the non-extendable dead time equation ($I_{true} = I_{obs}/(1-I_{obs}\tau$, where τ = dead time). If dead time is too small, then the true number of counts is underestimated. An error identical in sign, if not magnitude, can be introduced by errors in current measurement if the observed current (as recorded by an ammeter) is different from the actual current.

Figure 17 shows a series of Th and Pb count measurements in Trebilcock monazite and monazite 94-23 (Daniel and Pyle, in prep) at a variety of beam currents: 50, 100, and 200 nA for 94-25, and 10, 50, 100, 200, and 400 nA for Trebilcock. Each spot was measured three times at the same current in sample 94-25, and five times in Trebilcock. The beam was moved slightly within the same compositional domain, and the sequence was repeated again at a higher current. A systematic increase in count rate is noted for repeated spots at the same current, but the increase is within the statistical uncertainty of the analysis. Counting times were adjusted to keep analytical precision approximately constant.

For Pb on both spectrometers 4 and 5, normalized count rate is, within error, constant, regardless of analysis current (Figs. 17b–17f). For Th, however, there is a marked increase in normalized count rate with increasing current. In Trebilcock monazite, the normalized Th count rate increases from 12 cts/nA·s at 10 nA to 13.5 cts/nA·s at 100 nA, and is approximately constant thereafter (Fig. 17a). For 94-25, normalized Th count rate increases from 10.6 cts/nA·s at 50 nA to 12.9 cts/nA·s at 200 nA (Fig. 17d). The corresponding increase in Th concentration results in ages ranging from 1425 ± 23 Ma (1σ , avg. of 3 ages) at 50 nA to 1382 ± 9 Ma at 200 nA. For Trebilcock monazite, average age increases systematically with current as well, but the increase is not statistically significant.

The cause of the apparent increase in Th intensity with increasing current is unknown. An error in current measurement will affect measurements on all spectrometers proportionally; thus, errors in current measurement can be ruled out in the case of sample 94-25 (Figs. 17a and 17d). An erroneous dead time calculation for the counting circuitry associated with Th measurement could be to blame, but dead time effects at 3000–5000 cps are not likely (Geller and Herrington, 2002). Volatilization of lighter elements (P?) at high beam current, and corresponding increase in concentration of refractory elements, may be responsible, in part, for the apparent increase in Th intensity (e.g., Jercinovic and Williams 2005).

Pulse shift. The role of detector electronics in shaping and filtering voltage pulses passed to X-ray counters is discussed at

TABLE 5. Possible sources of inaccuracy in monazite chemical dating

Error source	Magnitude of error	Sign of error
Instrumental		
Dead time	1–2% relative	+
Current measurement	1–5% relative	±
Pulse shift	1–10% relative	+
d-spacing change	1–10% relative	-
Specimen		
Calibration standards	$\leq \sigma_{el}$ for Th, U, Pb	±
ZAF model	≤ 50 ppm Pb (?)	±
Variation in “fixed” ZAF elements	≤ 1 m.y. @ $\pm 2\sigma$, 2000 ppm Pb	±
ZAF factors at 15, 25 keV	$\Delta \text{age} \leq \sum \sigma_i^2 (i = \text{U, Th, Pb})$	±
Background measurement	Composition dependent; uni-directional variation of up to +150 m.y. has been recorded in replicate spot analyses using different backgrounds	±
Uncorrected peak interferences		
	1–2% relative in Proterozoic mnz	+
	1–15% relative in Paleozoic mnz	±
Orientation effects		
	Indeterminate	±
Surface effects		
	Appear to be $\leq \sigma_{el}$ for Th, U, Pb; larger for lighter elements (e.g., Y, P)	±

Notes: Sign of error: most common effect on calculated age indicated by symbol. + = increase calculated age; - = decrease calculated age; ± = generally indeterminate, or composition dependent.

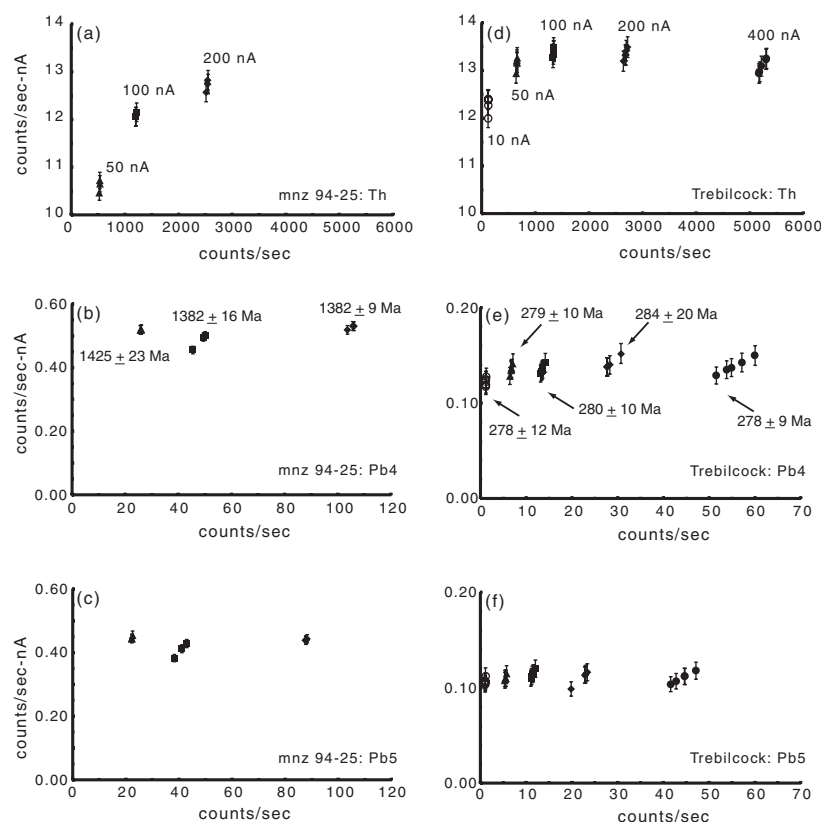


FIGURE 17. Plots of counts/s vs. counts/s·nA, for monazite, sample 94-25 (a,b,c) and Trebilcock monazite (d,e,f) at a variety of analytical currents. (a, d) Thorium counts. (b, e) Lead counts, spectrometer 4. (c, f) Lead counts, spectrometer 5. Error bars are ± 2 sigma counting statistics. Ages are quoted at ± 2 standard deviations. Sample 94-25 data from Pyle and Daniel (in prep).

length in Goldstein et al. (1984) and Scott et al. (1995). Detector gain and bias settings are adjusted so that when the spectrometer is tuned to a particular X-ray line, the voltage pulse produced by X-ray ionization of the detector gas is centered in the SCA voltage window. Voltage windows are typically run in differential mode to filter unwanted, higher-order reflections (e.g., Fig. 4).

Adoption of narrow voltage windows for pulse-height analysis, however, has the potential to generate a separate analytical problem relating to voltage pulse shift. Bertin (1970) and Goldstein et al. (1984) address the causes of pulse shift. Pulse distributions shift to lower voltages if count rates increase substantially, or to higher values if count rates decrease significantly. Count rate is proportional to analysis current, so pulse shift can be generated by large changes in current.

Typically, calibration and analysis are performed at the same high-value (50–250 nA) beam current (Scherrer et al. 2000, and references therein). In the case of an element present at trace levels in the unknown, and at high concentration in the standard, the potential exists for a pulse shift to higher voltage due to a significant count rate decrease. The setting of narrow voltage windows based on calibration PHA may therefore result in cutoff of some higher-voltage Pb signal during analysis. To prevent cutoff of high-voltage pulses (i.e., Pb signal), calibration current can be significantly lowered (e.g., from 200 nA to 10 nA) to minimize count rate change.

Adoption of low calibration current minimizes the chances of Pb signal clipping, but does leave the potential for voltage clipping of elements present in high concentrations in both

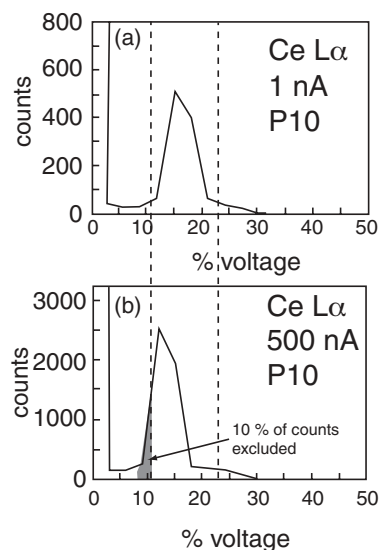


FIGURE 18. Single-channel analyzer (SCA) scans of Pb-doped (1.5 wt%) CePO₄ with spectrometer at CeL α ($n = 1$) position (a) SCA scan at low count-rate condition; voltage window optimized to include counts due to only CeL α X-rays. (b) SCA scan at high count-rate condition; increased count rate results in pulse shift to lower voltages (Goldstein et al. 1984), with the result that detector baseline and window settings reduce CeL α X-ray intensity by approximately 10%.

standards and natural monazite, such as Ce or Th. Concentrations of Ce in natural monazite are typically ~50% of the Ce concentration in CePO₄, and Th concentrations in metamorphic monazite approach 15–30% of the concentration level of Th in ThSiO₄. Centering the voltage window on the Ce pulse generated during calibration of CePO₄ (Fig. 18a) results in the loss of 10% of the Ce signal generated during analysis (Fig. 18b). For high-Th (≥15 wt%) monazite, setting minimum width windows during calibration results in loss of 3–5% of the Th signal from the unknown.

Voltage windows should be sufficiently narrow to filter higher-order peaks, yet wide enough to absorb possible pulse shift without clipping signal. Setting voltage windows requires knowledge of the expected count rate range (cps) for all elements during calibration, measurement of correction factors (Th, Y), and analysis. Table 6 lists calibration, correction measurement, and analysis count rate ranges for elements measured on the 733.

Changes in diffraction crystal interplanar spacing. Intermittent monitoring of Pb standard *k*-ratios reveals the presence and extent of spectrometer drift, such as that caused by temperature-related changes in diffraction crystal *d*-spacing (Fig. 3). Figure 19a shows a series of *k*-ratio measurements on the Pb standard PbSiO₃ over a three-hour period. Over that time, the average *k*-ratio has decreased by roughly 2%, meaning that the last measured unknown Pb concentrations are 2% less than if they had been measured just after calibration. Changes of ±6% in the Pb *k*-ratio have been recorded on the JEOL 733 at RPI (Figs. 19b–c). If temporal spectrometer drift is apparent, Pb concentrations should be corrected (Figs. 19b–19c) according to the time-dependent drift function (see Appendix 2).

Specimen errors (standard and unknown)

Specimen errors include, but are not limited to: (1) uncertainty in the composition of calibration standards, (2) absorption-enhancement, or ZAF, effects, (3) measurement of background intensity, (4) element interference, (5) orientation (shape and size) effects, and (6) surface effects. The discussion that follows

is germane to age analysis of monazite on any EMPA.

Uncertainty in composition of calibration standards. Accurate concentration values for Th, U, and Pb in their respective standards are crucial. Inaccuracies in the assumed concentrations

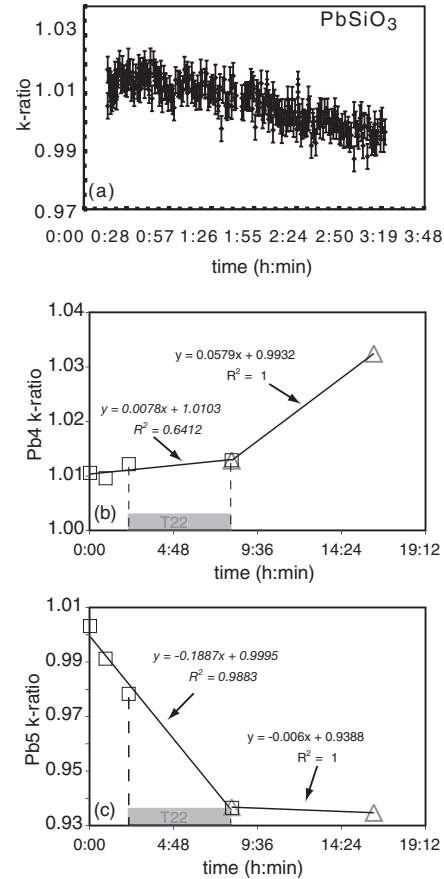


FIGURE 19. (a) Plot of *k*-ratio vs. time for measurements of PbMα *k*-ratio on Pb standard PbSiO₃; duration of experiment was approximately 3–¼ hours. Error bars are ±2σ. (b, c) Corrections for thermal expansion of PET diffraction crystal on spectrometer 4 and spectrometer 5, respectively. Each point is an average of five Pb *k*-ratio measurements on PbSiO₃. Both spectrometers experienced non-linear drift, which is modeled by dividing the overall analytical session into 2 segments. In each segment, drift is modeled as a linear function of time. Analysis segment 1 is indicated by black squares, and analysis segment 2 is indicated by gray triangles. Monazite from sample T22 (Table 13) was analyzed during segment 1, over the time interval indicated by the gray bar on the x-axis of both a and b, and the drift correction equations applied to lead measurement in T22 are italicized. Note that the mechanism responsible for drift causes an increase in *k*-ratio for spectrometer 4, but a decrease in *k*-ratio for spectrometer 5.

TABLE 6. Value range, peak counts per second, for measured elements in monazite chemical age analysis

Element and Line	gas	xtl	calibration, cps	correction factor, cps	analysis, cps
PbMα	Xe	PET	400–550	–	10–150
PbMβ	Xe	PET	350–550	–	10–100
UMβ	Ar	PET	600–1800	–	25–1050
ThMα	Ar	PET	250–800	~15 000	150–3500
YLα	Ar	TAP	4000–5000	~90 000	500–3500
CeLα	Ar	PET	~2500	–	8500–25000
SiKα	Ar	TAP	~1500	–	700–4000
CaKα	Ar	PET	~2400	–	300–3000

TABLE 7. Standards used in monazite chemical dating for this study

Element	Standard	Nominal elemental composition (wt%)	Standard: unknown ratio	Synthesis method
Y	YPO ₄	48.35% Y, 16.84% P, 34.80% O	10–100	REE(OH)gel, 1 atm non-Pb flux growth
Ce, P	CePO ₄	59.60% Ce, 13.18% P, 27.22% O	2–3, 0.95–1.05	REE(OH)gel, 1 atm non-Pb flux growth, REE(OH)gel, 10 kb piston-cylinder
Pb	PbSiO ₃	73.14% Pb, 9.91% Si, 16.94% O	50–5000	Pb, Si oxides, 1 atm melt/xtln
Th, Si	ThSiO ₄	71.59% Th, 8.67% Si, 19.74% O	3–30, 10–100	REE(OH)gel, 1 atm non-Pb flux growth
U	UO ₂	88.15% U, 11.85% O	30–500	REE(OH)gel, 1 atm non-Pb flux growth
Ca	Apatite	38.61% Ca, 12.80% P, 39.43% O, 3.43% F, 0.41% Cl, 0.17% Na, 0.16% Si	15–600	Natural Durango Apatite

of these elements in the standards will induce, through ZAF or $\phi\rho z$ corrections, proportional inaccuracies in calculated (U, Pb, Th) concentrations in the unknown. Of related interest in this case is the observation that the widely used LREEPO₄ standards synthesized with Pb₂P₂O₇ flux (Jarosewich and Boatner 1991), and containing 0.5–2.0 wt% PbO, do not produce uncertainties in: (a) U, Th and Pb concentrations, and (b) microprobe ages greater than uncertainties associated with elemental counting statistics (Donovan et al. 2003).

As natural mineral grains are commonly zoned, synthetic mineral standards, especially for Y, U, Th, and Pb, are preferred. Calibration standards for the elements measured in this microprobe dating protocol (Si, P, Ca, Y, Ce, Pb, Th, U) are listed in Table 7. Calcium is calibrated using well-characterized Durango apatite (Jarosewich et al. 1980); all other standards are synthetic oxides (U), phosphates (Ce, Y, P), or silicates (Th, Si).

ZAF corrections. The magnitude of, and errors associated with, ZAF or $\phi\rho z$ corrections can increase due to: (1) specific ZAF or $\phi\rho z$ correction applied; (2) significant variation in the concentration of element *i* in the unknown when the value of *i* is fixed for ZAF or $\phi\rho z$ corrections; (3) large deviations from unity for the value of the ratio $E_{i, std}/E_{i, unk}$; (4) large overvoltages (i.e., $E_{beam} - E_{critical}$, where E_{beam} is the beam accelerating voltage and $E_{critical}$ is the critical excitation energy of the analyzed X-ray line).

The quantification program dQant32 (Geller Microanalytical) used in conjunction with the 733 allows user selection of different

ZAF correction schemes, including Armstrong (1984), Heinrich (1985), Love/Scott (Sewell et al. 1985), Bastin et al. (1984), and Duncumb and Reed (1968). Each of these correction routines was applied to an analysis of Trebilcock monazite pre-corrected for element interference (Table 8a). The total variation in Pb concentration, ~50 ppm (Table 8), is less than the variation in Pb due to single-analysis 1 σ counting statistics, or approximately ± 85 ppm (Fig. 20a). The age spread encompassed by the different correction schemes (~15 m.y.) is approximately equal to the total (U+Pb+Th) compositional uncertainty (~15 m.y., 1 σ) due to statistical fluctuations (Fig. 20b). Thus, the error introduced by selection of different ZAF correction routines, in this case, is no larger than the error associated with the Pb statistical uncertainty of Trebilcock monazite.

The effect of elemental variation in monazite on ZAF-corrected U, Th, and Pb concentrations can be assessed by varying concentration of elements fixed (Table 2) for ZAF corrections. Table 8b shows the result of varying fixed element concentrations (La, Ce, Pr, Nd, Sm, Gd, Y, P, and O) by at least 2 standard deviations of the average monazite composition reported in Table 2. Age variation generated by changes in calculated U, Pb, and Th concentrations is on the order of ± 1 m.y.

Synthetic oxides, silicates, or phosphates of U, Th, Pb, etc. are typically homogeneous, with compositions known to a high degree of accuracy, which are both desirable qualities for calibration standards. However, element concentrations in the standard deviate significantly from the concentration range of the

TABLE 8a. Effect of ZAF corrections on chemical age (Fig. 22); Part I: model selection

Element	Th	U	Pb	Σ		
Compositional 1 σ (%)	0.83	1.58	5.15	5.45		
<i>k</i> -ratio	0.1378	0.005487	0.001679			
ZAF model	wt% Th	wt% U	wt% Pb	$\pm 2\sigma$ wt% Pb	Age Ma	$\pm 2\sigma$ age (10.9%)
Armstrong	11.46	0.5303	0.1671	± 0.0172	284	± 31
Heinrich	11.63	0.5350	0.1668	± 0.0172	280	± 31
Love/Scott I	11.65	0.5503	0.1697	± 0.0175	283	± 31
Bastin	11.51	0.5677	0.1696	± 0.0175	285	± 31
Duncumb/Reed	11.75	0.5989	0.1651	± 0.0170	270	± 29

TABLE 8b. Part II: variation in value of fixed element concentration; ZAF model used is Heinrich (1985)

	O	P	La	Ce	Pr	Nd	Sm	Gd	Y	U	Pb	Th	Age (Ma)
Std	26.66	13.03	12.00	25.20	2.50	10.60	1.63	1.35	1.2596	0.5406	0.1526	10.71	275
O=30	30.00	13.03	12.00	25.20	2.50	10.60	1.63	1.35	1.2595	0.5425	0.1526	10.74	274
P=15	26.66	15.00	12.00	25.20	2.50	10.60	1.63	1.35	1.2541	0.5426	0.1535	10.75	275
La=15	26.66	13.03	15.00	25.20	2.50	10.60	1.63	1.35	1.2612	0.5390	0.1523	10.68	275
Ce=30	26.66	13.03	12.00	30.00	2.50	10.60	1.63	1.35	1.2647	0.5386	0.1523	10.67	275
Pr=6	26.66	13.03	12.00	25.20	6.00	10.60	1.63	1.35	1.2644	0.5395	0.1525	10.69	275
Nd=15	26.66	13.03	12.00	25.20	2.50	15.00	1.63	1.35	1.2668	0.5394	0.1526	10.69	275
Sm=5	26.66	13.03	12.00	25.20	2.50	10.60	5.00	1.35	1.2691	0.5400	0.1529	10.70	275
Gd=5	26.66	13.03	12.00	25.20	2.50	10.60	1.63	5.00	1.2677	0.5403	0.1528	10.71	275

Note: Bold indicates varied element.

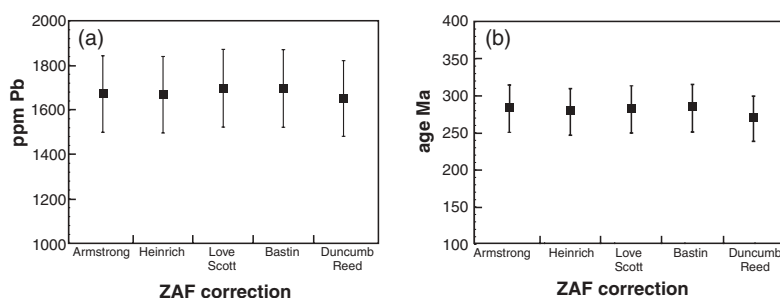


FIGURE 20. Uncertainties associated with selection of various ZAF correction models. (a) Uncertainty in Pb concentration. (b) Uncertainty in age. ZAF correction models are those of Armstrong (1984), Heinrich (1985), Sewell et al. (1985), Bastin et al. (1984), and Duncumb and Reed (1968). Error bars in both graphs are $\pm 2\sigma$.

analogous element in the unknown. Table 7 shows the $E_{l_{std}}/E_{l_{unk}}$ ratio typical for this combination of standards and metamorphic monazite. Unless primary standards with REE, Pb, Th, and U concentrations approximating those found in natural monazite are used, large values of the ratio $E_{l_{std}}/E_{l_{unk}}$ are unavoidable. Selection of standards for monazite analysis is discussed at length in Scherrer et al. (2000) and Pyle et al. (2002); the latter paper addresses standard selection with respect to the magnitude of ZAF corrections generated by a particular standard set and unknown. For typical monazite compositions, $PbSiO_3$ generates slightly smaller $ZAF_{unknown}/ZAF_{standard}$ ratios than crocoite or pyromorphite (Pyle et al. 2002).

A survey of the literature (Scherrer et al. 2000, and references therein) shows accelerating voltages adopted for monazite analysis range from 15–25 keV. Scott et al. (1995) suggest adoption of accelerating voltages of 2–3 times the critical excitation energy of the analyzed element. For a given current and analysis duration, higher accelerating voltages increase X-ray intensity and analysis precision. However, higher beam energies also increase excitation volume (cf., Fig. 1). The other negative effect of adopting a 25 keV accelerating voltage is a large ZAF correction associated with large overvoltages for the *M* lines of Pb, U, and Th ($E_{critical}$ 2.5–3.5 keV).

To assess the effect of accelerating voltage on precision, ZAF correction factors, and calculated U, Th, and Pb concentrations, Trebilcock monazite was analyzed in duplicate at accelerating voltages of 15 and 25 keV. Analytical lines, background offsets, cup current, and counting times were not varied in either set of analyses. At 25 keV (Table 9) the standard-normalized (i.e.,

$ZAF_{Trebilcock}/ZAF_{Std}$) corrections for the unknown are 1.71 (Y), 1.35 (Pb), 1.14 (Th), and 1.12 (U). Adoption of a 15 keV accelerating voltage slightly increases the corrections for Th (1.14) and U (1.17), but significantly decreases the absolute corrections for both Y (1.26) and Pb (1.22).

Ages at 15 and 25 keV are given in Table 10 (Parts I and II). Yttrium concentration increases, on average by 5% from 25 to 15 keV, U increases by 7%, Pb by 1.5% on spectrometer 4 and 4.5% on spectrometer 5. Average Th and Ce concentrations change by less than 0.5%. The average ages ($n = 15$) are 286 Ma (25 keV) and 288 Ma (15 keV) for Pb as measured on spectrometer 4, and 284 Ma (25 keV) and 293 Ma (15 keV) for Pb as measured on spectrometer 5. Differences in both pairs of average ages are not statistically significant at 2σ (Table 11). For 15 keV analyses, 1σ uncertainties increase, on average, approximately 25% relative to 25 keV uncertainties.

Modeling and measurement of background. As Figures 10–11 and 13–14 indicate, the method selected for interpolation of background intensity at the measured peak position is a major component of the overall accuracy of monazite microprobe ages. The examples presented in Figures 10, 11, 13, and 14 show the variation inherent in different background fits for monazites of low (2.5%) to moderately high (11%) Th content. Increase in calculated Pb concentration for a variety of background fits is sufficient to increase the calculated age by as much as 20 m.y. in Trebilcock (Fig. 10) and 40 m.y. for Xe detectors (or 70 m.y. for Ar detectors) in T22 (Fig. 11). In these two examples, variations in calculated U concentration for different background fits have a statistically insignificant effect on the calculated age. However, for Th-rich samples, interpolated background values at the $UM\beta$ peak will be significantly affected by the type of background fit, and the location of background measurement relative to both Th *M* lines (*M3-N4*, *M5-P3*, *M4-O2*) and the *ThM4* and *M5* absorption edges. Background collection on the short-wavelength side of *ThMγ* in Th-rich monazite will typically result in an underestimation of $UM\beta$ background intensity, overestimation of U concentration, and spuriously young ages.

Element interference. Uranium and Pb peak and background-region interferences are listed in Table 3. If the interferences are uncorrected, significant inaccuracy can result. The difference between uncorrected and interference-corrected age is a function of the concentrations of Th, U, Pb, and Y (for $PbM\alpha$), or Ce (for $PbM\beta$), and is maximized for high-Th and -Y, low-U, juvenile (low-Pb) monazites. Examples in Table 11 show that interference correction decreases age by 1–2% in mid-Proterozoic monazites (94-27, 00-2A) and 10–15% in mid-Paleozoic monazites from samples BF-64, TM-637 (Pyle and Spear, unpublished), and Trebilcock monazite. Uncorrected interferences on background collection positions (see above) will result in underestimation of the true concentrations of U and Pb; such interferences should be corrected in a manner analogous to peak interference correction.

Orientation (shape and size) effects. Small, irregularly shaped grains, or grains with high inclusion densities, may generate X-rays that pass through media with dissimilar ZAF properties before exiting the sample and traveling to the diffracting crystal (e.g., Fig. 2).

A series of traverses on Trebilcock monazite mounted in

TABLE 9. ZAF factors (standard and unknown at 15 and 25 keV accelerating voltage)

Element (standard)	Z	A	F	ZAF	Bks corr
Part I: 25 keV					
Ce (CePO ₄)	1.1087	0.9433	1.0000	1.0459	0.8322
Y (YPO ₄)	1.1066	0.9284	1.0000	1.0274	0.8642
Th (ThSiO ₄)	1.0800	0.9047	1.0000	0.9771	0.7188
U (UO ₂)	1.0298	0.9344	1.0000	0.9622	0.6432
Pb (PbSiO ₃)	1.0782	0.9583	1.0000	1.0333	0.7224
Element (Trebilcock)				ZAF_{Treb}/ZAF_{std}	Bks corr
Ce (CePO ₄)	1.0989	1.0054	0.9992	1.1039	1.0555
Y (YPO ₄)	1.0341	1.7020	0.9980	1.7566	1.7097
Th (ThSiO ₄)	1.1487	0.9737	0.9996	1.1180	1.1442
U (UO ₂)	1.1482	0.9392	0.9995	1.0788	1.1202
Pb (PbSiO ₃)	1.1436	1.2170	0.9999	1.3915	1.3466
Part II: 15 keV					
Element (standard)					Bks corr
Ce (CePO ₄)	1.1697	0.9744	1.0000	1.1397	0.8762
Y (YPO ₄)	1.1206	0.9607	1.0000	1.0765	0.8647
Th (ThSiO ₄)	1.1271	0.9445	1.0000	1.0645	0.7524
U (UO ₂)	1.0533	0.9620	1.0000	1.0132	0.6884
Pb (PbSiO ₃)	1.1041	0.9665	1.0000	1.0671	0.7383
Element (Trebilcock)				ZAF_{Treb}/ZAF_{std}	Bks corr
Ce (CePO ₄)	1.1550	0.9997	0.9994	1.1540	1.0126
Y (YPO ₄)	1.0345	1.3134	0.9988	1.3572	1.2608
Th (ThSiO ₄)	1.2291	0.9761	0.9997	1.1995	1.1268
U (UO ₂)	1.2369	0.9609	0.9997	1.1881	1.1727
Pb (PbSiO ₃)	1.1911	1.0897	0.9999	1.2979	1.2162

Note: Bks corr = backscatter correction coefficient.

TABLE 10. Comparison of 15 keV and 25 keV age data, Trebilcock monazite

Part I – 25 keV																		
Calibration and correction information																		
Date	el	no. cal	C/nA·s	s	nA (cup)	1-σ (%)	CF Pb interference		CF U interference									
3/04	Y	3	470.00	20	10.03	0.48	0.003479 Pb4 (1), 0.003186 Pb5 (1)		–									
3/04	Ce	3	277.71	20	10.04	0.45	–		–									
3/04	U	3	190.91	20	10.02	0.53	–		–									
3/04	Th	4	84.82	20	9.99	0.78	0.001736 Pb4 (1), 0.001522 Pb5 (1)		0.002954 (1)									
3/04	Pb4	4	63.96	20	10.02	0.89	–		–									
3/04	Pb5	4	58.56	20	10.02	0.93	–		–									
Analysis information																		
Trebilcock monazite																		
No.	Ce	Th	Y	U*	Pb4*	Pb5*	2σ U (%)	2σ Th (%)	2σ Pb4 (%)	2σ Pb5 (%)	Age 4 Ma	2σ	Age 5 Ma	2σ	Avg spot age Ma	Exp spot 2σ	Exp spot 2 s.e.	n
1	17.13	11.34	17328	5361	1787	1775	3.84	1.90	7.44	7.60	306	26	304	27	305	26	18	2
2	17.26	11.23	17318	5203	1643	1623	3.94	1.86	7.94	8.14	285	26	282	26	283	26	18	2
3	17.05	11.33	17967	5366	1670	1675	3.82	1.86	7.72	7.96	286	25	287	26	287	26	18	2
4	17.14	11.30	17774	5343	1662	1685	3.84	1.86	7.80	7.92	286	25	290	26	288	26	18	2
5	17.24	11.26	17852	5311	1754	1638	3.88	1.86	7.50	8.14	303	26	283	26	293	26	18	2
6	17.27	11.30	17896	5428	1714	1631	3.82	1.86	7.66	8.20	294	26	280	26	287	26	18	2
7	17.27	11.31	17966	5264	1641	1710	3.92	1.86	7.88	7.84	283	25	294	26	288	26	18	2
8	17.01	11.29	17866	5345	1695	1635	3.88	1.86	7.72	8.20	292	26	281	26	287	26	18	2
9	17.06	11.34	17942	5452	1653	1585	3.80	1.86	7.86	8.38	283	25	271	25	277	25	18	2
10	17.04	11.50	17607	5444	1680	1540	3.80	1.86	7.80	8.58	284	25	260	25	272	25	18	2
11	17.07	11.41	17607	5354	1547	1706	3.86	1.86	8.30	7.94	264	25	291	26	277	26	18	2
12	17.08	11.20	17942	5423	1676	1666	3.82	1.88	7.88	8.08	290	26	288	26	289	26	18	2
13	17.05	11.39	18140	5360	1739	1636	3.86	1.86	7.56	8.30	297	26	279	26	288	26	18	2
14	17.16	11.33	18173	5350	1438	1581	3.86	1.86	8.86	8.46	247	24	271	26	259	25	18	2
15	17.02	11.39	17923	5238	1682	1584	3.94	1.86	7.80	8.46	288	26	271	26	280	26	18	2

Spectrometer 4 average (n = 15): 286 ± 29 Ma (2σ), 286 ± 8 Ma (2 std. err)

Spectrometer 5 average (n = 15): 284 ± 21 Ma (2σ), 284 ± 5 Ma (2 std. err)

Grand average (n = 30): 285 ± 25 Ma (2σ), 285 ± 5 Ma (2 std. err)

Part II – 15 keV																		
Calibration and correction information																		
Date	el	no. cal	C/nA·s	s	nA (cup)	1-σ (%)	CF Pb interference		CF U interference									
3/04	Y	3	302.37	20	10.07	0.65	0.004370 Pb4 (1), 0.003954 Pb5 (1)		–									
3/04	Ce	3	105.70	20	10.12	0.71	–		–									
3/04	U	3	100.74	20	10.02	0.73	–		–									
3/04	Th	3	47.25	20	10.02	1.05	0.001844 Pb4 (1), 0.001466 Pb5 (1)		0.005934 (1)									
3/04	Pb4	3	38.55	20	10.03	1.15	–		–									
3/04	Pb5	3	34.89	20	10.03	1.21	–		–									
Analysis information																		
Trebilcock monazite																		
No.	Ce	Th	Y	U*	Pb4*	Pb5*	2σ U (%)	2σ Th (%)	2σ Pb4 (%)	2σ Pb5 (%)	Age 4 Ma	2σ	Age 5 Ma	2σ	Avg spot age Ma	Exp spot 2σ	Exp spot 2 s.e.	n
1	17.07	11.36	18506	5734	1624	1643	4.96	2.36	9.84	10.22	276	31	279	32	277	32	23	2
2	17.12	11.30	18418	5707	1558	1723	4.96	2.34	10.30	9.84	266	31	294	33	280	32	23	2
3	17.18	11.34	18768	5887	1684	1831	4.84	2.34	9.56	9.28	285	31	310	33	297	32	23	2
4	17.05	11.38	18687	5450	1783	1552	5.16	2.34	9.22	10.66	304	33	265	32	284	32	23	2
5	17.08	11.32	18681	5829	1724	1697	4.88	2.34	9.52	9.92	293	32	288	33	290	32	23	2
6	17.20	11.22	18719	5645	1544	1733	5.00	2.34	10.34	9.72	265	31	298	33	281	32	23	2
7	17.22	11.32	18798	5603	1637	1670	5.04	2.34	9.92	10.10	279	32	285	33	282	32	23	2
8	17.05	11.36	18556	5429	1756	1682	5.14	2.32	9.42	10.00	300	33	287	33	294	33	23	2
9	17.01	11.27	18636	5998	1713	1874	4.78	2.34	9.58	9.18	291	32	318	34	304	33	23	2
10	17.08	11.30	18503	5752	1739	1715	4.90	2.34	9.46	9.86	296	32	292	33	294	32	23	2
11	16.90	11.22	18622	5853	1695	1597	4.86	2.34	9.70	10.42	290	32	273	32	281	32	23	2
12	17.05	11.30	18575	5586	1669	1891	5.06	2.34	9.80	9.10	285	32	323	34	304	33	23	2
13	17.20	11.24	18748	5974	1599	1605	4.78	2.34	10.18	10.38	272	31	273	32	273	32	23	2
14	17.02	11.33	18561	5664	1867	1760	5.00	2.34	9.04	9.72	318	34	299	33	308	34	24	2
15	17.01	11.14	18842	5876	1779	1811	4.86	2.34	9.34	9.44	306	33	311	34	308	34	24	2

Spectrometer 4 average (n = 15): 288 ± 30 Ma (2σ), 288 ± 8 Ma (2 std. err)

Spectrometer 5 average (n = 15): 293 ± 34 Ma (2σ), 284 ± 9 Ma (2 std. err)

Grand average (n = 30): 291 ± 32 Ma (2σ), 291 ± 5 Ma (2 std. err)

Notes: Ce and Th concentrations given in wt% element, all others in ppm element. U*, Pb4*, and Pb5* are concentrations of U, Pb4 (spectrometer 4 measurement) and Pb5 (spectrometer 5 measurement) corrected for Th and Y interference.

epoxy (Figs. 21a–c) were performed to test whether spectrometer orientation relative to traverse orientation has an effect on measured *k*-ratios. Spectrometer orientation is shown at the upper part of each panel. The grain was rotated approximately 60° for each set of line traverses, which included traverses in the grain interior, parallel to the grain edge, and perpendicular to and crossing over the grain edge. In traverse 4, for example (Fig. 21b), X-rays reaching spectrometer 2 pass largely through the monazite grain, whereas X-rays reaching spectrometers 3, 4, and 5 pass largely through epoxy.

The traverses (Fig. 21d) show that if the X-ray path to the spectrometer passes through epoxy, the apparent concentration increases as the grain boundary is approached. For traverse 4, the X-ray travel path to spectrometers 3, 4, and 5 passes through epoxy, and apparent Pb concentration, as measured by these spectrometers, increases toward the grain boundary. The same travel path applies for traverse 5, as well. For traverse 8, the X-

ray travel path to spectrometer 3 is largely through monazite, and the apparent concentration of Pb as measured by spectrometer 3 decreases, whereas the apparent Pb concentration as measured by spectrometers 2, 4, and 5 increases.

In general, any X-ray travel path that reaches the spectrometer through a material with smaller Z and A corrections than those of monazite (quartz, mica, etc.) will result in an increase in apparent Pb (or Th and U) concentration. The magnitude of the change is severe for a monazite-epoxy grain boundary. Traverse 4 displays an apparent Pb concentration increase of 66%, traverse 8 displays an increase of 100%, and traverse 8, 133%. The low *k*-ratios on spectrometer 2, traverse 4, may be a result of *d*-spacing change of the PET crystal associated with spectrometer 2.

Although these increases are extreme because epoxy is highly transparent to X-rays, monazite X-rays passing through quartz at grain boundaries or quartz inclusions may experience a diminished equivalent of the monazite-epoxy phenomenon. The X-rays

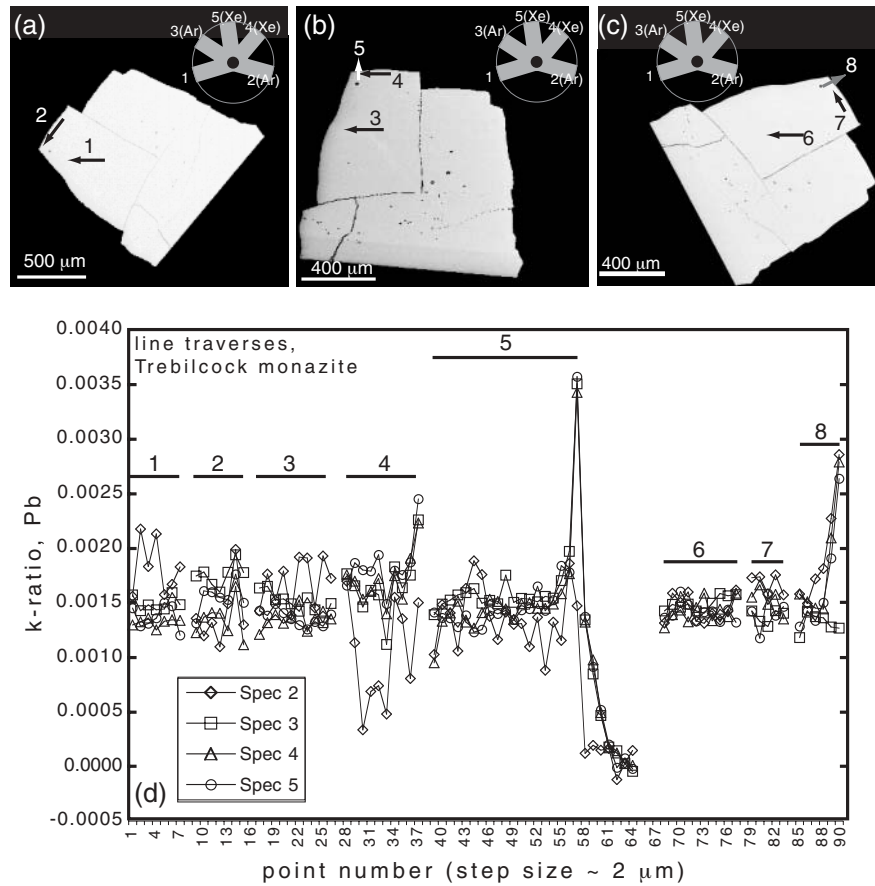


FIGURE 21. BSE images of Trebilcock monazite depicting a series of traverses (a,b,c), each with a different grain orientation, to investigate possible relationships between grain/spectrometer orientation, edge effects/spectrometer orientation, and calculated compositions. Approximate orientation of the five spectrometers shown on each panel. Direction of traverse indicated by arrow – numbers on traverse line relate to line plot shown in b. (b) Line plot of Pb *k*-ratio for individual point analyses in Trebilcock monazite. Number above traverses 1–8 correlated with traverse lines 1–8 on a. Step size in each traverse is approximately 2 μm, and Pb *k*-ratios are collected simultaneously on spectrometers 2 (diamonds), 3 (squares), 4 (triangles), and 5 (circles). *K*-ratio increase or decrease at monazite-epoxy boundary is a function of orientation of spectrometer relative to both grain edge and traverse orientation.

TABLE 11. Magnitude of correction for interference, and effect on age

Sample	Analysis	Raw Th	Raw Y	Raw U	Raw Pb	Raw age	Corr U	Corr Pb	Corr age	Δ%
94-27 low Th	98	37300	10549	15153	5938	1421	15042	5848	1408	0.91
00-2A high Th/U	12	97800	10728	21779	11136	1389	21487	10968	1377	0.86
00-2A low Th/U	19	23028	8547	4007	2487	1452	3939	2423	1426	1.79
BF-64 high Th	3a	108800	13714	5975	2453	427	5570	2167	382	10.5
BF-64 low Th	5	32700	3956	3312	720	371	3191	636	331	10.8
TM-637	4	24100	10729	5158	725	397	5069	631	349	12.9
Trebilcock	3	112800	19339	5726	1844	314	4929	1534	267	14.96

Note: Concentration in ppm, age in Ma.

of all elements present will be affected, but to different degrees, based on the mass-absorption coefficients of the individual element X-rays for the specific non-monazite absorber, and the overall form of the ZAF or $\phi\rho z$ correction. An estimate of the error introduced to age estimates by this effect is speculative unless the process is modeled within a ZAF or $\phi\rho z$ correction. Such a model must include mass-absorption coefficients and other relevant input data for both the presumed and actual absorbers. Monazite grains displaying complex zoning may be cryptically zoned in Th, U, or Pb on a scale smaller than the resolution of the electron beam. This fact, combined with small grain size and/or orientation factors, may lead to inter-spectrometer age variation greater than the expected statistical deviation. Additionally, the effect noted here would be more severe at 25 keV due to the larger excitation volume of the electron beam.

Given typical monazite grain size, morphology, and tendency to include other phases, an ideal monazite analysis excluding edge effects or inclusion effects may be difficult to realize. Recognition of these factors may help to explain systematically significant differences in multi-spectrometer ages, or spurious ages unexplainable by any other means.

Surface effects. Surface effects such as roughness, conductive coat degradation, or beam damage can alter calculated concentration through scattering effects, absorption effects, or actual loss of volatile elements (evaporation, melting) in monazite.

Use of Pb-free polishing media is essential in preparation of monazite for microprobe dating, as Pb-bearing polishing disks deposit Pb within cracks and along grain boundaries. Lead-free laps, as described by Scherrer et al. (2000), remove the risk of introducing contaminant Pb during polishing. An alternative to mechanical polishing of monazite is chemical-mechanical polishing (CMP) with a colloidal silica suspension. The high pH (9–10) of the suspension enhances sample surface reactivity, and suspended silica particles with a size distribution of 0.05–0.07 μm impart an ultrahigh-quality polish. CMP polishing produces an exceptionally flat grain boundary polish (Figs. 22a and 22b) and is well suited for enhancing grain-boundary alteration features such as those present in monazite T22 (Fig. 22c).

The use of different coating materials (C, Au, Al), and their response to a high-current focused electron beam has been treated at length by Jercinovic and Williams (2005), who noted spotting of carbon-coated surfaces and a concomitant decrease in P concentration for long-duration (10 min), high-current (200 nA), focused beam analyses.

For this study, only carbon coats of 200–300 Å thickness (checked against coated brass) were used. The electron beam was defocused slightly (6–8 μm), and analysis current was maintained at approximately 200 nA. Degradation of carbon coat and surface damage was noted in some cases, but surface or carbon-coat response varied from grain to grain within the same sample. Figure 23 shows two monazite grains from the same sample analyzed at identical conditions. Each of the two spots in both grains experienced roughly 30 minutes of beam exposure; the grain in Figure 23a shows only minor spotting, whereas the grain in Figure 23b appears to have melted. The grains are compositionally similar; the only difference in surface properties is a large fracture present beneath the analysis pits shown in Figure 23b. Clearly, response to beam irradiation is

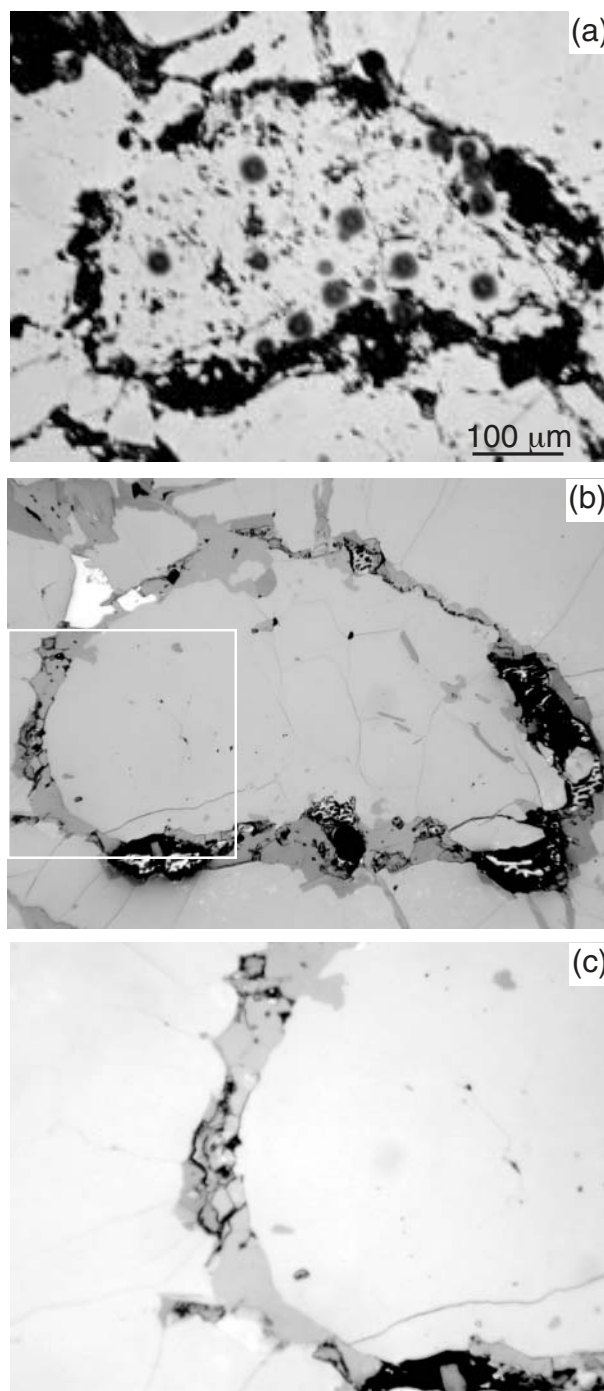


FIGURE 22. Image of pre- and post- colloidal silica polishing of monazite from sample T22. (a) Reflected light photomicrograph of monazite inclusion in garnet, with surface pitting and plucked grain boundaries. Large dark spots are ion-beam pits. Polish shown is 1 μm diamond paste finish. (b) Same grain after 4-hour treatment with colloidal silica chemical-mechanical polishing. A large portion of the plucked monazite grain boundaries have been smoothed by polishing. (c) Enlarged image of left-hand monazite grain boundary.

unique to a particular monazite grain, and must be monitored on a grain-to-grain basis if carbon is the material selected for the conductive coat.

Overall accuracy

Systematic errors including machine-related (spectrometer drift, pulse shift, dead time) and sample-related (sample damage, size/orientation/composition effects, ZAF corrections, background, element interference) issues can significantly affect the monazite microprobe age, especially if the errors are additive. In a worst case scenario, additive errors from Th pulse clipping (5–7% loss of Th), temperature change and the resulting increase in Pb *k*-ratio (5–7%), monazite grain edge effects, resulting in artificially boosted Pb concentration (5–7%), and incorrectly estimated background intensity (1–10%) increase the apparent Pb concentration by 15–30%. This increase is in addition to random fluctuations about the true age, which are largely dependent on Pb counting statistics. It is also assumed that (1) standard compositions are known perfectly, and (2) interference corrections are performed correctly; if not, the error will be greater.

Age inaccuracies arising from systematic errors can be reduced greatly by performing pulse-height analysis for all measured elements on both standards and individual composi-

tional domains in natural monazite, scanning at least one peak and background ROI for each distinct monazite compositional domain, and periodic monitoring for spectrometer drift during analysis, with subsequent correction. If pulse clipping is eliminated, spectrometer drift corrected, background is modeled as accurately as possible, and elemental interference is corrected, the remaining systematic errors (dead time, error/uncertainty in ZAF correction models, imprecise knowledge of standard composition) impart further uncertainties equal to or less than overall analytical uncertainty. Furthermore, suspect analyses should be discarded if: (1) conductive coat or sample surface damage from beam irradiation results in multi-analysis, same-spot compositional variation of greater than 3σ, or (2) edge, size, orientation, or inclusion effects introduce spurious ZAF corrections.

The identification and minimization of systematic errors is crucial to the microprobe dating process, as these errors may not be obvious in the calculated age, due to compensatory cancellation. For example, the following three pairs of systematic errors act to offset changes in the calculated age: (1) clipping of Th voltage pulse (-Th) and interference on Pb background (-Pb); (2) non-correction of $YL\gamma_{2,3}$ interference on $PbM\alpha$ (+Pb) and misplacement of background collection position for U with respect to $ArK\alpha$ absorption edge (+U); (3) time-dependent Pb spectrometer drift (-Pb) and monazite-quartz edge effect on ZAF correction (+Pb); and (4) incorrectly modeled background for $UM\beta$ (-) and $PbM\alpha$ (-) in a high-Th (~20%) monazite. Such systematic error pairs can shift from additive to compensatory

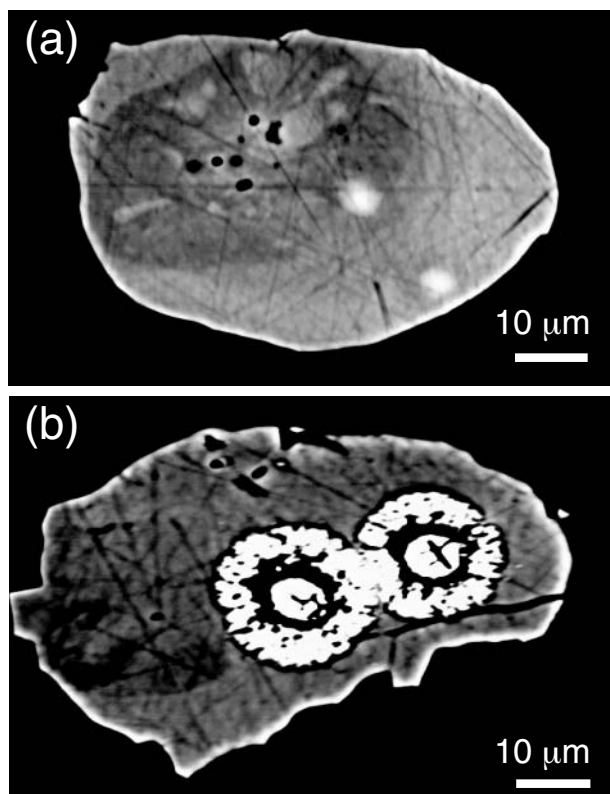


FIGURE 23. BSE intensity image showing beam damage to monazite surface. Both grains (a) and (b) are from the same thin section, and were analyzed at identical conditions (~200 nA cup current, 25 keV accelerating voltage, 6–8 μm beam diameter) for approximately 30 minutes of continuous analytical time per spot (5 spots at 6 minutes each).

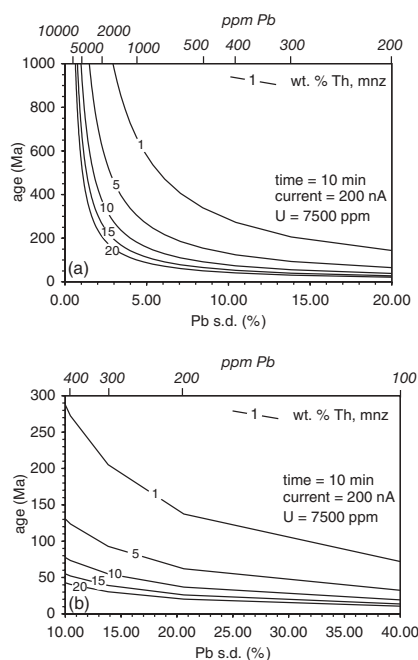


FIGURE 24. Plot of Pb precision and concentration vs. age for an intrinsic X-ray detector response [sealed Xe detector (4), PET diffraction crystal] measured on the JEOL 733 Superprobe at RPI. For calculation of the figure, analytical time and current were fixed at 600 s and 200 nA. (a) Plot for Pb analytical standard deviations of 0–20%. Plot for Pb analytical standard deviations of 10–40%. Both plots incorporate a fixed U concentration of 7500 ppm. Precision curves are calculated for monazites with Th concentrations of 1, 5, 10, 15, and 20 wt.%.

within a single grain, as composition, position, and cumulative analysis time change.

DISCUSSION

Selection of single-analysis analytical tolerance

Once systematic errors are minimized to the largest extent possible, the precision of a single-analysis “date” is a function of (1) total U + Th + Pb content, (2) analysis current, and (3) analysis time. By varying Th and Pb concentrations for a fixed U concentration and a particular X-ray detector response, microprobe ages at maximum acceptable analytical tolerance

$$\left(\sqrt{\epsilon_U^2 + \epsilon_{Th}^2 + \epsilon_{Pb}^2}\right) \quad (5)$$

can be calculated for any combination of Th concentration and analytical conditions (current and time).

For a 10 minute, 200 nA analysis, monazites with ≥ 1000 ppm Pb (Fig. 24a) have an inherently high analytical precision (1σ RSD of 5% or less). If the Pb 1σ RSD of 5% precision (composition) is taken as limiting, a precision-limited age of 600 Ma is imposed for a monazite with 1% Th and 7500 ppm U, and a precision-limited age of 90 Ma is imposed for a monazite with 20 wt.% Th and 7500 ppm U. Tolerance of lower precisions (Fig. 24b) decreases the precision-limited age accordingly; adoption of a limiting Pb 1σ RSD of 20%, or approximately 220 ppm Pb, yields single-analysis precision-limited ages of $\sim 140 \pm 56$ Ma (2σ) for a monazite with 1% Th and 7500 ppm, and $\sim 20 \pm 8$ Ma (2σ) for a monazite with 20% Th and 7500 ppm U. It should be noted, however, that dates associated with maximum acceptable analytical tolerances are essentially independent of precisions associated with the ages of separate monazite domains, as non-temporal data (composition, texture) are typically used to classify such domains.

Worked example

The U, Th, Pb concentrations and microprobe ages presented thus far in this paper demonstrate several attempts to identify a “best” monazite dating protocol, or to at least quantify the errors associated with varying the critical dating protocol parameters, such as detector gas, accelerating voltage, beam diameter, de-

tector electronics, analytical line, background offsets, etc. Application of these parameters should be checked against unique monazite compositional domains identified within a sample. The variation in spectral characteristics from domain to domain highlights the need to map individual monazite grains, prior to age analysis, for element distribution.

Due to the lack of U-Th-total Pb age standards, monazite microprobe ages are typically checked against isotopic age determinations of the same material (e.g., Williams et al. 1999). For comparison, we present age results from monazite T22 (Spear et al., in revision). Analytical parameters for the T22 analyses (25 keV) are given in Table 12. Composition and age results for T22 are listed in Table 13.

The monazite from sample T22 has two distinguishable compositional domains (Figs. 25a, and 25c-25e), a core region of low Th (2–3 wt% ThO₂) and U (0.3–0.5 wt% UO₂) overgrown by a discontinuous rim of high Th (~6–9 wt% ThO₂) and U (1–2 wt% UO₂). Fifty single-cycle spot age analyses were performed on this grain (Fig. 25b), yielding 100 dates (Table 13).

Lead analytical precisions (Table 13) range from 7–15%, or ± 17 –34 m.y. (1σ), for core analyses, and 3–7%, or ± 13 –17 m.y. (1σ) for rim analyses. The average propagated analytical uncertainty for a single analytical cycle is ± 88 Ma (2σ) for core analyses and ± 46 Ma (2σ) for rim analyses (Fig. 26a). Weighted average ages for the core (418 ± 10 Ma, $n = 62$, 2 s.e.) and rim (423 ± 6 , $n = 38$, 2 s.e.) domains are statistically indistinguishable. Summation of probability curves for single-spectrometer ages generates pseudo-Gaussian histograms (Fig. 26b). The most probable age bins (bin width = 4 m.y.) in each histogram are 424 Ma for the core domain, and 428 Ma for the rim domain.

Spear et al. (in revision) measured ²⁰⁸Pb/²³²Th ages for the core ($n = 9$) of this grain, and obtained an average ²⁰⁸Pb/²³²Th core age of 430 ± 3 Ma (1σ). This value is slightly older than the average microprobe age. However, P-B background calculations for the core of the grain (see Fig. 11) suggest that exponential fit to background 1, or a low background on the short-wavelength side of PbMβ (Figs. 9 and 11), increases the calculated Pb concentration such that the age increases by 9–12 Ma (430–434 Ma). Such an age increase places the microprobe age in agreement with the ²⁰⁸Pb/²³²Th isotopic age.

TABLE 12. EMPA settings for monazite chemical age calibration and analysis, protocol no. 1a (25 keV), no. 1b (15 keV)

Element (spec)	crystal	gas	peak	Gain (V)	Bias(V)	Baseline(V)	Window(V)	high bkg (+mm)	low bkg (-mm)	Max Peak time (s)	Max total Background time (s)
Part I: calibration: 25 keV, 10 nA (no. 1a): 15 keV, 10 nA (no. 1b)											
Y (1)	TAP	Ar	Lα	12	1693	11	50	1.20	1.60	100	100
Ce (2)	PET	Ar	Lα	7	1680	23	58	4.00	3.00	10	10
Th (3)	PET	Ar	Mα	7	1725	15	35	4.00	4.00	80	80
U (3)	PET	Ar	Mβ	6	1735	15	45	4.00	3.00	80	80
Pb4 (4)	PET	Xe	Mα	20	1810	20	35	6.27	12.73	180	180
Pb5 (5)	PET	Xe	Mα	20	1810	15	35	6.27	12.73	180	180
Part II: analysis 25 keV, 200 nA (no. 1a): 15 keV, 10 nA (no. 1b)											
Y (1)	TAP	Ar	Lα	12	1693	11	50	1.20	1.60	100	100
Ce (2)	PET	Ar	Lα	7	1680	23	58	1.50	1.50	10	10
Th (3)	PET	Ar	Mα	7	1725	15	35	2.70	3.00	80	80
U (3)	PET	Ar	Mβ	6	1735	15	45	2.50	3.00	80	80
Pb4 (4)	PET	Xe	Mα	20	1810	20	35	6.27	3.90	180	180
Pb5 (5)	PET	Xe	Mα	20	1810	15	35	6.27	3.90	180	180

Notes: spec = spectrometer number; Pb4 = lead measured on spectrometer 4; Pb5 = lead measured on spectrometer 5. Detector settings are specific to the JEOL 733 Superprobe EMP at Rensselaer Polytechnic Institute. Background offsets are for a 140 mm Rowland circle. Trebilcock (Table 10, part I) and T22 (Table 13) analyses were performed with protocol no. 1a (25 keV). Trebilcock analyses listed in Table 10, part II, were performed with protocol no. 1b (15 keV).

TABLE 13A. Chemical age analyses of monazite from Cavendish formation, Star Hill, Vermont, USA (Sample T22)

Calibration and correction information								
Date	el	no. cal	C/nA-s	s	nA (cup)	1σ (%)	CF Pb interference	CF U interference
2/03	Y	3	503.2	30	10.03	0.29	0.003749±0.000166 Pb4 (3), 0.003466±0.000077 Pb5 (3)	-
2/03	Ce	3	267.5	30	10.02	0.37	-	-
2/03	U	4	187.0	30	10.03	0.43	-	-
2/03	Th	3	83.8	30	10.03	0.64	0.001738±0.000062 Pb4 (3), 0.001469±0.000043 Pb5 (3)	0.002806 (3)
2/03	Pb4	5	58.3	30	10.03	0.76	-	-
2/03	Pb5	5	49.8	30	10.03	0.82	-	-

TABLE 13B. Analysis info T22 monazite 1, analyzed 2/14/2003 (Pb/Mo analysis)

Analysis info.																
(domain)	Th	Y	U*	Pb4*	Pb5*	2σ U (%)	2σ Th (%)	2σ Pb4 (%)	2σ Pb5 (%)	Age 4 (Ma)	2σ (m.y.)	Age 5 (Ma)	2σ (m.y.)	Spot avg age (Ma)	Expected spot 2σ (m.y.)	Expected Spot 2 s.e. (m.y.)
1 (c)	2.20	bdl	4247	750	673	4.76	1.96	18.84	20.78	438	86	419	90	429	88	62
2 (c)	2.24	bdl	3589	709	528	5.64	1.96	20.20	26.60	433	91	347	95	390	93	66
3 (c)	2.06	bdl	3580	659	552	5.62	2.04	21.52	25.70	426	95	383	101	405	98	69
4 (c)	2.04	bdl	2936	574	484	6.76	2.04	24.50	29.12	397	101	362	108	379	105	74
5 (r)	5.78	bdl	3555	1381	1224	5.46	1.64	10.86	11.88	405	50	394	52	400	51	36
6 (r)	5.68	bdl	14581	2278	2010	1.82	1.64	6.72	7.72	461	33	431	35	446	34	24
7 (r)	5.39	bdl	2074	1323	1141	8.86	1.62	11.08	12.60	444	63	420	65	432	64	45
8 (r)	7.44	bdl	2137	1681	1569	8.48	1.64	8.88	9.32	418	52	430	55	424	53	38
9 (r)	5.59	bdl	2063	1386	1137	8.98	1.62	10.54	12.68	451	63	405	63	428	63	45
10 (r)	6.55	bdl	2151	1331	1322	8.52	1.64	11.04	11.10	367	52	407	57	387	54	39
11 (c)	2.35	bdl	4082	699	716	5.00	1.92	20.52	20.10	395	84	434	90	414	87	62
12 (c)	2.24	bdl	3443	870	617	1.96	5.86	16.32	23.22	544	95	411	99	477	97	68
13 (r)	5.50	bdl	1665	1157	968	10.72	1.62	12.48	14.42	385	64	358	65	371	64	45
14 (c)	2.39	bdl	3918	740	648	5.22	1.92	19.18	21.96	420	84	395	90	408	87	61
15 (c)	2.56	bdl	4076	755	736	5.04	1.86	18.96	19.64	403	79	423	86	413	83	59
16 (c)	3.39	bdl	4361	948	715	4.70	1.70	15.34	20.04	407	66	334	69	370	67	48
17 (c)	3.43	bdl	4150	930	895	4.94	1.68	15.52	16.26	401	66	418	71	409	69	48
18 (c)	3.07	bdl	3825	924	884	5.30	1.74	15.44	16.38	444	73	457	79	451	76	54
19 (r)	5.91	bdl	9026	1716	1701	2.56	1.64	8.78	8.98	402	37	429	41	416	39	28
20 (c)	2.45	bdl	3757	763	666	5.38	1.90	18.62	21.62	432	84	405	91	419	87	62
21 (c)	2.26	bdl	3793	778	589	5.36	1.96	18.34	24.38	466	90	378	95	422	92	65
22 (c)	2.17	bdl	3590	736	651	5.66	2.00	19.48	22.42	461	94	435	101	448	97	69
23 (r)	6.78	6651	5701	1688	1468	3.72	1.64	8.98	10.10	392	39	380	41	386	40	28
24 (r)	7.04	bdl	9809	2142	2027	2.40	1.64	7.26	7.74	435	34	442	37	438	35	25
25 (r)	6.90	bdl	9863	1935	1892	2.40	1.64	7.38	8.24	427	34	418	37	423	35	25
26 (r)	6.86	bdl	10232	2018	1871	2.32	1.64	7.14	8.34	442	34	410	36	426	35	25
27 (r)	6.88	bdl	9530	1889	2050	2.44	1.64	7.58	7.68	423	34	458	38	440	36	25
28 (r)	7.00	bdl	6549	1612	1585	3.28	1.64	8.66	9.58	395	37	388	40	391	38	27
29 (r)	7.03	bdl	10244	1998	1951	2.32	1.64	7.20	8.02	430	33	421	36	426	35	24
30 (r)	5.46	bdl	15060	2052	2003	1.80	1.62	7.10	7.98	442	33	432	36	437	35	24
31 (r)	4.00	3026	1043	716	808	16.82	1.62	17.52	17.50	369	90	416	101	392	95	68
32 (r)	7.18	bdl	9322	1987	1945	2.48	1.64	7.22	8.04	434	34	425	36	430	35	25
33 (c)	2.59	bdl	3902	676	758	5.24	1.86	19.64	19.42	392	80	438	89	415	84	60
34 (r)	5.72	bdl	17447	2165	2294	1.64	1.64	6.72	7.02	424	30	449	33	437	32	22
35 (c)	3.08	bdl	4427	924	925	4.68	1.74	14.66	16.08	456	71	456	77	456	74	52
36 (c)	2.32	bdl	3580	629	544	5.66	1.94	21.08	26.88	404	89	350	96	377	92	65
37 (c)	2.47	bdl	3790	646	663	5.40	1.90	20.54	22.08	390	83	400	91	395	87	62
38 (c)	2.43	bdl	3476	640	652	5.84	1.90	20.86	22.68	402	87	409	96	405	92	65
39 (c)	2.77	bdl	4018	724	646	5.10	1.82	18.18	22.40	397	75	355	82	376	79	56
40 (c)	2.50	bdl	3709	676	781	5.50	1.88	19.66	18.90	407	84	469	93	438	88	62
41 (c)	2.36	bdl	3796	745	724	5.38	1.94	18.00	20.26	462	87	450	95	456	91	64
42 (c)	2.46	bdl	3900	744	752	5.24	1.90	18.00	19.66	445	84	450	92	447	88	62
43 (c)	2.34	bdl	3986	759	588	5.18	1.94	17.82	24.82	465	87	363	92	414	89	63
44 (c)	2.25	bdl	4074	785	490	5.04	1.96	17.18	29.28	488	88	308	92	398	90	64
45 (c)	2.37	bdl	3821	685	739	5.34	1.94	19.54	20.04	424	86	456	95	440	91	64
46 (c)	2.42	bdl	3956	707	755	5.18	1.90	19.08	19.52	426	85	454	92	440	88	62
47 (c)	2.58	bdl	4253	766	649	4.86	1.86	17.58	22.62	431	79	367	85	399	82	58
48 (c)	2.50	bdl	3977	694	726	5.14	1.90	19.28	20.44	409	82	428	91	419	86	61
49 (c)	2.28	bdl	3863	723	723	5.30	1.96	18.56	20.58	456	89	456	97	456	93	66
50 (c)	2.45	bdl	3932	734	588	5.20	1.90	18.38	24.98	440	84	354	90	397	87	62

Notes: standard deviations for correction factor are at ±1σ; number of analyses averaged to produce correction factor listed in parentheses. Concentrations listed in ppm, except for Th (wt%); bdl = below detection limits. c = core analysis, r = rim analysis. Weighted average core age: 418 Ma ± 10 Ma (2 s.e.), n = 62; weighted average rim age: 423 Ma ± 6 Ma (2 s.e.), n = 38. For the same domains, weighted average ²⁰⁸Pb/²³²Pb ages are 430 ± 2 Ma (core, n = 9), 442 ± 8 Ma (rim, n = 12) (2 s.e.) (Spear et al. in revision).

CONCLUDING REMARKS

Microprobe dating of monazite has been shown to be an extremely useful adjunct to traditional isotopic dating. Given

the extreme variability in monazite composition, and the composition-dependent sensitivity of the precision and accuracy of this method, it is recognized that no one microprobe dating

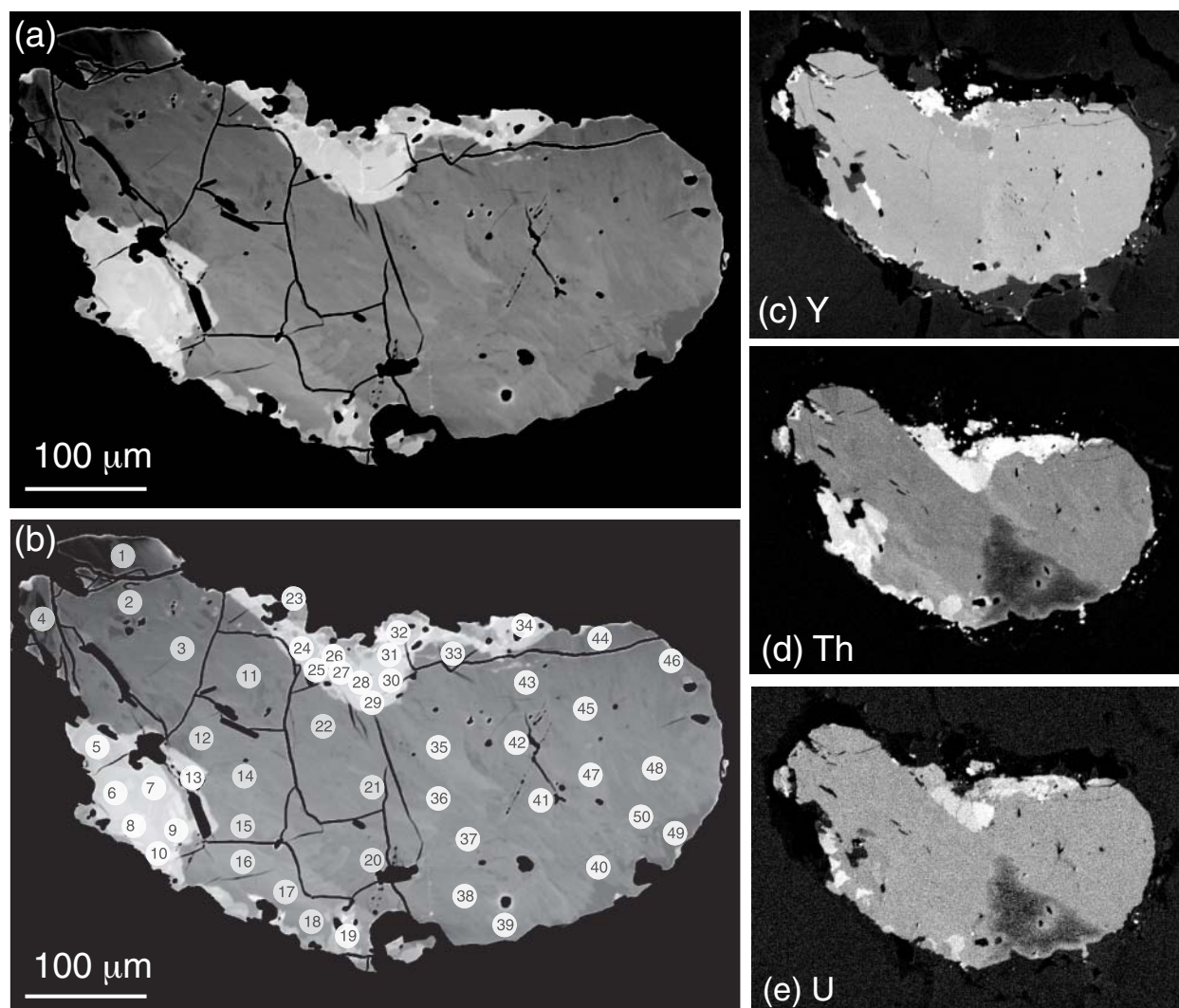


FIGURE 25. (a) BSE intensity image of monazite inclusion in garnet, sample T22. (b) image from a with analysis positions (Table 13) labeled. Size of analytical label is approximately twice the beam diameter used in analysis. Yttrium, Th, and U distribution maps for this grain are shown in (c), (d), and (e), respectively. Triangular dark patches in d and e were caused by deprecipitation of carbon coat during element mapping routine.

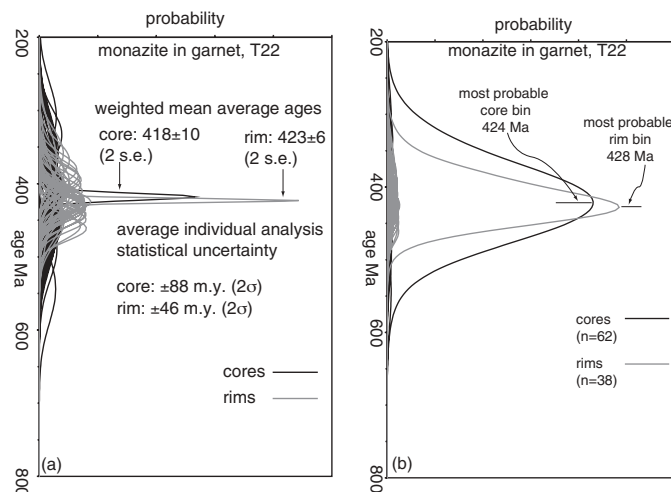


FIGURE 26. Graphic representations of individual age analyses, monazite T22. (a) Individual ages plotted as Gaussian curves with a mean value given by the measured age (2 ages per spot) and a standard deviation given by the quadratic sum of the analytical uncertainties in U, Th, and Pb. Core domain ages are shown as black curves, and rim domain ages are shown as gray curves. The decreased width of the rim domain Gaussian curves ($2\sigma = \pm 46$ m.y.) relative to the core domain curves ($2\sigma = \pm 88$ m.y.) is due to the higher Th and U content of the rim domain. The core and rim domains have weighted average ages (± 2 standard errors of the mean) of 418 ± 10 Ma ($n = 62$) and 423 ± 6 Ma ($n = 68$), respectively. (b) Age results from monazite T22 re-cast as a pseudo-Gaussian histogram, with bin widths of 4 m.y. The histograms for the core (black) and rim (gray) domains are generated by summing the individual probability curves in each domain.

protocol will optimize Pb analytical precision. Instead, flexibility in parameters such as background collection position, beam diameter, analytical current, and analysis duration is warranted. This paper has emphasized the role of detector gas in affecting analytical precision, and the difficulties attached to analysis of Pb with 1-atm Ar detectors coupled with 140 mm Rowland circles. Many of the problems cited in the text are reduced or eliminated with high-pressure (≥ 2 atm) Ar detectors (Jercinovic and Williams 2005), or larger-radius Rowland circles. EMPAs with 1-atm Ar detectors and 140 mm Rowland circles can obtain Pb analyses at the accuracy level of Xe detectors, provided care is taken in fitting background and accounting for the presence of second-order LREE escape peaks. Regardless of the type of X-ray detector used, careful attention to the form and modeling of background radiation in the U and Pb *M*-line regions of WD spectra is absolutely crucial for an acceptable degree of accuracy in monazite microprobe age determinations.

Current EMPA development emphasizes the incorporation of high-intensity diffraction crystals, improved stage movement resolution, and increased beam current at lower accelerating voltages. Such additions will improve analysis precision while reducing sample damage. However, rigorous evaluation of the accuracy of monazite microprobe age determinations requires synthesis and complete chemical and crystallographic characterization of (U, Th, Pb)-bearing monazite age standards. Production of such a standard is the next step in improving this technique.

ACKNOWLEDGMENTS

We thank Kiera Becker for maintenance of and assistance on the JEOL 733 Superprobe at RPI. Thanks also go to Mike Williams and Mike Jercinovic (University of Massachusetts, Amherst) for organizing the Monazite Microprobe Geochronology short course at UMass in March of 2002, and to M.W. M.J., and Bob Tracy (Virginia Polytechnic Institute) for organizing the special session at the GSA 2002 annual meeting in Denver, Colorado. The free exchange of ideas and materials between our lab and the UMass group (Williams, Jercinovic, P. Goncalves, K. Mahan) has helped both groups in their attempts to tackle this important and intriguing analytical problem. Comprehensive and constructive reviews by Mike Jercinovic and Pete Dahl aided in significantly improving the first draft of this paper, and the editorial handling of Mike Williams is greatly appreciated, as well.

REFERENCES CITED

Armstrong, J.T. (1984) Quantitative analysis of silicate and oxide minerals: a re-evaluation of ZAF corrections and proposal for new Bence-Albee coefficients. *Microbeam Analysis-1984*, 19, 208–212.

Asami, M., Suzuki, K., and Grew, E.S. (2002) Chemical Th-U-total Pb dating by electron microprobe analysis of monazite, xenotime and zircon from the Archean Napier Complex, east Antarctica: evidence for ultra-high-temperature metamorphism at 2400 Ma. *Precambrian Research*, 114, 249–275.

Bertin, E.P. (1970) *Principle and Practice of X-Ray Spectrometric Analysis*. Plenum Press, New York.

Bastin, G.F., van Loo, F.J.J., and Heijligers, H.J.M. (1984) An evaluation of the use of Gaussian prc curves in quantitative electron probe microanalysis. *X-Ray Spectrometry*, 13, 91–97.

Bevington, P.R. (1969) *Data Reduction and Error Analysis for the Physical Sciences*. McGraw-Hill, New York.

Cherniak, D.J., Watson, E.B., Grove, M., and Harrison, T.M. (2004) Pb diffusion in monazite: a combined RBS/SIMS study. *Geochimica et Cosmochimica Acta*, 68, 829–840.

Cho, K.-H., Takgaki, H., and Suzuki, K. (1999) CHIME monazite age of granitic rocks in the Sungehang shear zone, Korea; timing of dextral ductile shear. *Geoscience Journal (Seoul)*, 3, 1–15.

Cocherie, A. and Albarede, F. (2001) An improved U-Th-Pb age calculation for electron microprobe dating of monazite. *Geochimica et Cosmochimica Acta*, 65, 4509–4522.

Daniel, C.G. and Pyle, J.M. (2002) Monazite thermochronometry in kyanite + sillimanite \pm andalusite-bearing schists and from the Picuris Range, northern New Mexico. *Geological Society of America, Abstracts with Programs*, 34, 172 (Paper 76-3).

Donovan, J.J., Hanchar, J.M., Piccoli, P.M., Schrier, M.D., Boatner, L.A., and Jarosewich, E. (2003) A re-examination of the rare earth element orthophosphate reference samples for electron microprobe analysis. *Canadian Mineralogist*, 41, 221–232.

Duncumb, P. and Reed, S.J.B. (1968) The calculation of stopping power and backscattering effects in electron microprobe analysis. In K.F.J. Heinrich, Ed., *Quantitative Electron Microprobe Analysis*, National Bureau of Standards Special Publication 298, 133–154. U.S. Department of Commerce, Washington, D.C.

Geller, J.D. and Herrington, C. (2002) High count rate electron probe microanalysis. *Journal of Research of the National Institute of Standards and Technology*, 107, 503–508.

Goldstein, J., Newbury, D., Echlin, P., Joy, D., Fiori, D., and Lifshin, E. (1984) *Scanning Electron Microscopy and X-Ray Microanalysis*. Plenum, New York.

Grew, E.S., Suzuki, K., and Asami, M. (2001) CHIME ages of xenotime, monazite, and zircon from beryllium pegmatites in the Napier complex, Khmara Bay, Enderby Land, East Antarctica. *Polar Geoscience*, 14, 99–118.

Harlov, D.E. and Förster, H.-J. (2003) Fluid-induced nucleation of (Y+REE)-phosphate minerals within apatite: nature and Experiment. Part II. Fluorapatite. *American Mineralogist*, 88, 1209–1229.

Heinrich, K.F.J. (1985) A simple accurate absorption model. *Microbeam Analysis-1985*, 20, 79–81.

Jarosewich, E. and Boatner, L.A. (1991) Rare-earth element reference samples for electron microprobe analysis. *Geostandards Newsletter*, 15, 397–399.

Jarosewich, E., Nelen, J.A., and Norberg, J.A. (1980) Reference samples for electron microprobe analysis. *Geostandards Newsletter*, 4, 43–47.

Jenkins, R. and DeVries, J. (1982) *Practical X-ray Spectrometry*. Springer Verlag, Berlin.

Jercinovic, M.J. and Williams, M.L. (2005) Analytical perils (and progress) in electron microprobe trace element analysis applied to geochronology: background acquisition, interferences, and beam irradiation effects. *American Mineralogist*, 90, 526–546.

Johann, H.H. (1931) Die Erzeugung lichstarker Röntgenspektren mit Hilfe von Konkavkristallen. *Zeitschrift für Physik*, 69, 185–206.

Johannson, T. (1933) Über ein neuartiges genau fokussierendes Röntgenspektrometer. *Zeitschrift für Physik*, 82, 507–528.

Karioris, F.G., Gowda, K., and Cartz, L. (1991) Heavy ion bombardment on monoclinic ThSiO₄, ThO₂, and monazite. *Radiation Effects Letters*, 58, 1–3.

Kim, B.-C., Choi, S.-J., Suzuki, K., Adachi, M., Obayashi, T., and Yu, K.-M. (1997) Provenance of Cretaceous sandstones in the southeastern Youngdong Basin, Korea: CHIME geochronology of detrital monazites. *Geoscience Journal (Seoul)*, 1, 37–49.

Krohe, A. and Wawrzenitz, N. (2000) Domainal variations of U-Pb monazite ages and Rb-Sr whole-rock dates in polymetamorphic paragneisses (KTB drill core, Germany): influence of strain and deformation mechanisms on isotope systems. *Journal of Metamorphic Geology*, 18, 271–291.

Meldrum, A., Boatner, L.A., and Ewing, R.C. (1997) Displacive radiation effects in the monazite- and zircon-structure orthophosphates. *Physics Reviews B*, 56, 13805–13814.

Montel, J.-M., Foret, S., Veschambre, M., Nicollet, and Provost, A. (1996) Electron microprobe dating of monazite. *Chemical Geology*, 131, 37–53.

Pan, Y. and Stauffer, M.R. (2000) cerium anomaly and Th/U fractionation in the 1.85 Ga Flin Flon paleosol: clues from REE- and U-rich accessory minerals and implications for paleoatmospheric reconstruction. *American Mineralogist*, 85, 898–911.

Parrish, R.R. (1990) U-Pb dating of monazite and its application to geological problems. *Canadian Journal of Earth Sciences*, 27, 1431–1450.

Pyle, J.M. (2001) Distribution of select trace elements in pelitic metamorphic rocks: pressure, temperature, mineral assemblage, and reaction-history controls. Ph.D. dissertation, Rensselaer Polytechnic Institute.

Pyle, J.M. and Spear, F.S. (2003) Four generations of accessory-phase growth in low-pressure migmatites from SW New Hampshire. *American Mineralogist*, 88, 338–351.

Pyle, J.M., Spear, F.S., and Wark, D.A. (2002). Electron microprobe analysis of REE in apatite, monazite, and xenotime: protocols and pitfalls. In M.L. Kohn, J. Rakovan, and J.M. Hughes, Eds., *Phosphates—Geochemical, Geobiological, and Materials Importance*, 48, 337–362. *Reviews in Mineralogy and Geochemistry*, Mineralogical Society of America, Washington, D.C.

Pyle, J.M., Spear, F.S., Cheney, J.T., and Layne, G. (2005) Monazite ages in the Chesham Pond Nappe, SW New Hampshire: implications for assembly of central New England thrust sheets. *American Mineralogist*, 90, 592–606.

Reed, S.J.B. and Buckley, A. (1996) Virtual WDS. *Mikrochimica Acta*, 13, 479–483.

Scherrer, N.C., Engi, M., Gnos, E., Jakob, V., and Leichti, A. (2000) Monazite analysis; from sample preparation to microprobe age dating and REE quantification. *Schweizerische Mineralogische und Petrographische Mitteilungen*, 80, 93–105.

Scott, V.D., Love, G., and Reed, S.J.B. (1995) *Quantitative Electron-Probe Microanalysis (second edition)*. Ellis Horwood Ltd, Chichester.

Sewell, D.A., Love, G., and Scott, V.D. (1985) Universal correction procedure for

- electron-probe microanalysis. I. Measurement of X-ray depth distributions in solids. *Journal of Physics D*, 18, 1233–1243.
- Siegbahn, J. (1931) *Spektroskopie der Röntgenstrahlen* (second edition). Springer, Berlin.
- Spear, F.S. and Pyle, J.M. (2002) Apatite, xenotime, and monazite in metamorphic rocks. In M.L. Kohn, J. Rakovan, and J.M. Hughes, Eds., *Phosphates—Geochemical, Geobiological, and Materials Importance*, 48, 293–335. *Reviews in Mineralogy and Geochemistry*, Mineralogical Society of America, Washington, D.C.
- Suzuki, K. and Adachi, M. (1991) Precambrian provenance and Silurian metamorphism of the Tsonosawa paragneiss in the South Kitakami terrane, northeast Japan, as revealed by the chemical Th-U-total Pb isochron ages of monazite, zircon, and xenotime. *Geochemical Journal*, 25, 357–376.
- Suzuki, K., Adachi, M., and Kajizuka, I. (1994) Electron microprobe observations of diffusion in metamorphosed detrital monazites. *Earth and Planetary Science Letters*, 128: 391–405.
- Tomaschak, P.B., Krogstad, E.J., and Walker, R.J. (1996) U-Pb monazite geochronology of granitic rocks from Maine: implications for late Paleozoic tectonics in the northern Appalachians. *Journal of Geology*, 104, 185–195.
- Wendt, I. and Carl, C. (1991) The statistical distribution of the mean squared weighted deviation. *Chemical Geology*, 86, 1991.
- Williams, M.L. and Jercinovic, M.J. (2002) Microprobe monazite geochronology: putting absolute time into microstructural analysis. *Journal of Structural Geology*, 24, 1013–1028.
- Williams, M.L., Jercinovic, M.J., and Terry, M.P. (1999) Age mapping and dating of monazite on the electron microprobe: deconvoluting multi-stage histories. *Geology*, 27, 1023–1026.

MANUSCRIPT RECEIVED APRIL 12, 2003

MANUSCRIPT ACCEPTED OCTOBER 31, 2004

MANUSCRIPT HANDLED BY MICHAEL WILLIAMS

APPENDIX 1. PROPAGATION OF ANALYTICAL UNCERTAINTIES IN Pb AND U CONCENTRATIONS CORRECTED FOR INTERFERENCE

Considering solely peak intensity, $PbM\alpha$ yields a more precise analysis than $PbM\beta$. However, the interferences on both Pb peaks decrease analytical precision, as the corrected Pb concentration is a function of the interfering elements, each of which carries analytical uncertainty. To determine whether a corrected $PbM\alpha$ analysis (with Th and Y interference) is less precise than a interference-free $PbM\beta$ analysis, the analytical uncertainties in the measured and interfering elements must be propagated through the equation for interference-corrected concentration. Standard error propagation techniques are given in Bevington (1969), and, in this case, all covariance terms are assumed to be zero.

Correction for interference of element x on element y requires measurement of the apparent concentration of element y in the y -free standard for element x . The correction factor for the interference of x on y (CF_{x-y}) is calculated as:

$$CF_{x-y} = y_{k-ratio}^{std,x} / x_{k-ratio}^{std,x} \sim y_{k-ratio}^{std,x} \quad (A1-1)$$

and the corrected concentration in the unknown is calculated as:

$$y_{corr(wt\%)}^{unk} = y_{uncorr(wt\%)}^{unk} - (CF_{x-y}) (x_{k-ratio}^{unk}) \quad (A1-2a)$$

or, alternately:

$$y_{corr(k-ratio)}^{unk} = y_{uncorr(k-ratio)}^{unk} - (CF_{x-y}) (x_{k-ratio}^{unk}) \quad (A1-2b)$$

The difference in application of Equation A1-2a vs. A1-2b to correct for interference is negligible, as long as k -ratios, and not concentrations, are used for both the correction factor and the interfering element in the unknown. Application of A1-2b

requires application of a ZAF correction after the interference correction is made, whereas A1-2a does not. In the case of $PbM\alpha$ and $UM\beta$, an equation of the form of A1-2a or A1-2b is used, and the correction factor is summed over the interference contributions from Th ($M\zeta_{1,2} + M2-O4$) and $YL\gamma_{2,3}$ for $PbM\alpha$, and Th ($M\gamma + M5-P3 + M3-N4$) for $UM\beta$, namely:

$$conc_{Pb^*,unk} = conc_{Pb,unk} - [(CF_{Th-Pb}) \cdot conc_{Th,unk} + (CF_{Y-Pb}) \cdot conc_{Y,unk}] \quad (A1-3a)$$

$$conc_{U^*,unk} = conc_{U,unk} - [(CF_{Th-U}) \cdot conc_{Th,unk}] \quad (A1-3b)$$

It should be noted that each concentration is a k -ratio with an applied ZAF correction, and the k -ratio itself is the ratio of counts in the unknown divided by counts in the standard. Thus, the correction factor is simply a ratio of k -ratios.

$$CF_{Th-Pb} = \frac{k-rat_{Pb,Th_std@200nA}}{k-rat_{Th,Th_std@200nA}} = \frac{\frac{cts_{Pb,Th_std@200nA}}{cts_{Pb,Pb_std@10nA}}}{\frac{cts_{Th,Th_std@200nA}}{cts_{Th,Th_std@10nA}}} \quad (A1-4)$$

The correction factors are measured at 200 nA (to replicate analysis conditions), but are ratioed (or k -ratioed) to the calibration measurement of that element at 10 nA; this variation of current between calibration and analysis of unknown is reflected in the subscripts in Equation A1-4. Likewise, the correction factors for the other interferences may be represented as:

$$CF_{Th-Y} = \frac{k-rat_{Pb,Y_std@200nA}}{k-rat_{Y,Y_std@200nA}} = \frac{\frac{cts_{Pb,Y_std@200nA}}{cts_{Pb,Pb_std@10nA}}}{\frac{cts_{Y,Y_std@200nA}}{cts_{Y,Y_std@10nA}}} \quad (A1-5)$$

$$CF_{Th-U} = \frac{k-rat_{U,Th_std@200nA}}{k-rat_{Th,Th_std@200nA}} = \frac{\frac{cts_{U,Th_std@200nA}}{cts_{U,U_std@10nA}}}{\frac{cts_{Th,Th_std@200nA}}{cts_{Th,Th_std@10nA}}} \quad (A1-6)$$

In addition to the correction factors, the concentrations of Pb, Th, U, and Y must be factored into the expression for corrected concentration. Because the raw intensities of U and Pb are subject to interference from Th and Y, an estimate of the corrected Pb and U intensities must be made using equations analogous to (A1-3a) and (A1-3b), substituting intensities (in units of counts/nA·s) for concentration. Thus, the analytical precision of the corrected intensities will be slightly lower than that of the uncorrected U and Pb intensities.

The concentrations (k -ratios) of U and Pb are functions of the intensities of *both* standards and unknown. Although the Pb intensity in the unknown is not an explicit function of Th intensity in the Th standard, the correction factor for Pb is an explicit function of Th intensity in the Th standard, as well as Y intensity in the Y standard. Therefore, the expression for analytical precision of Pb corrected for elemental interferences may include terms representing the analytical precision of the interferences in their respective standards.

The corrected Pb analytical precision is calculated as follows. First, the raw Pb intensity (cts/nA·s) in the unknown is corrected for Th and Y interference, using analogues of Equation A1-3a or A1-3b. Second, the precision in this corrected Pb intensity is calculated:

$$\sigma_{Pb,krat} = \sqrt{\sigma_{Pb,unk}^2 + \sigma_{Pb,std}^2} \quad (A1-7)$$

Each of the terms under the radical is determined with the following formula:

$$\left(\frac{\sqrt{\frac{P}{I^2t^2} + \frac{B}{I^2t^2}}}{\frac{P}{It} - \frac{B}{It}} \right) \cdot 100 \quad (A1-8)$$

Where P = peak counts, B = background counts, I = current (nA) and t = time (s). Thus, the precision in the *corrected* Pb analysis ($\sigma_{Pb^*,krat}$) is of the following form:

$$\sigma_{Pb^*,krat} = \sigma_{Pb,krat} + f(\text{equation A1-3a}) \quad (A1-9)$$

If it is assumed that concentration_{unknown} \equiv k -ratio_{unknown} \equiv (counts unknown/counts standard), then (A1-3a) can be rewritten as

$$\frac{cts_{Pb^*,unk@200nA}}{cts_{Pb^*,Pb_std@10nA}} = \frac{cts_{Pb,unk@200nA}}{cts_{Pb,Pb_std@10nA}} - \left[\left(\frac{cts_{Pb,Th_std@200nA}}{cts_{Pb,Pb_std@10nA}} \right) \bullet \frac{cts_{Th,unk@200nA}}{cts_{Th,Th_std@10nA}} + \left(\frac{cts_{Pb,Y_std@200nA}}{cts_{Pb,Pb_std@10nA}} \right) \bullet \frac{cts_{Y,unk@200nA}}{cts_{Y,Y_std@10nA}} \right] \quad (A1-10)$$

and

$$\frac{cts_{U^*,unk@200nA}}{cts_{U^*,U_std@10nA}} = \frac{cts_{U,unk@200nA}}{cts_{U,U_std@10nA}} - \left[\left(\frac{cts_{U,Th_std@200nA}}{cts_{U,U_std@10nA}} \right) \bullet \frac{cts_{Th,unk@200nA}}{cts_{Th,Th_std@10nA}} \right] \quad (A1-11)$$

The error in the corrected concentration of Pb is therefore a function of:

- Uncorrected counts of Pb in the unknown at 200 nA = (a)
- Counts of Pb in the Pb standard at 10 nA = (b)
- Counts of Pb in the Th standard at 200 nA = (c)
- Counts of Th in the Th standard at 200 nA = (d)
- Counts of Th in the Th standard at 10 nA = (e)
- Counts of Th in the unknown at 200 nA = (f)
- Counts of Pb in the Y standard at 200 nA = (g)
- Counts of Y in the Y standard at 200 nA = (h)

- Counts of Y in the Y standard at 10 nA = (i)
- Counts of Y in the unknown at 200 nA = (j)

Each one of the terms above has a corresponding uncertainty ($\sigma_a, \sigma_b, \dots, \sigma_j$). Taking Equations A1-9 and A1-10, recasting the corrected concentration of Pb as the unknown variable “y”, and making the substitutions (a, b, c, etc.) above yields

$$y = a + b - \left[\left(\frac{c}{d} \right) \cdot \frac{f}{e} + \left(\frac{g}{h} \right) \cdot \frac{j}{i} \right] \quad (A1-12)$$

The only difference between A1-9 and A1-12 is that the term associated with the uncorrected k -ratio of Pb in the unknown ($\sigma_{Pb,krat}$) in A1-9 has been expanded to include its implicit dependence on uncorrected Pb counts in the unknown (a), and Pb counts in the Pb standard (b). Expanding Equation A1-12 yields:

$$y = a + b - \frac{cef}{bed} - \frac{gij}{bih} = a + b - \frac{cf}{bd} - \frac{gj}{bh} \quad (A1-13)$$

From the expansion, it is apparent that the Pb precision corrected for Th and Y interference is *not* a function of counts of Th in the Th standard measured at 10 nA (term “e”), nor of counts of Y in the Y standard measured at 10 nA (term “i”). Thus, for interfering elements, only the precisions as measured in the unknown, and for the correction factors, are used to calculate the corrected Pb precision.

The uncertainty in the Pb analysis corrected for Th and Y interference (σ_y) is a function of the 8 independent variables (a-d, f-h, j) in A1-13. If all covariances are assumed to equal zero, then the uncertainty σ_y may be calculated by standard error propagation techniques (e.g., Bevington 1969):

$$\sigma_y^2 = \left(\frac{\partial y}{\partial a} \right)^2 \sigma_a^2 + \left(\frac{\partial y}{\partial b} \right)^2 \sigma_b^2 + \left(\frac{\partial y}{\partial c} \right)^2 \sigma_c^2 + \left(\frac{\partial y}{\partial d} \right)^2 \sigma_d^2 + \left(\frac{\partial y}{\partial f} \right)^2 \sigma_f^2 + \left(\frac{\partial y}{\partial g} \right)^2 \sigma_g^2 + \left(\frac{\partial y}{\partial h} \right)^2 \sigma_h^2 + \left(\frac{\partial y}{\partial j} \right)^2 \sigma_j^2 \quad (A1-14)$$

Differentiating A1-13 with respect to y gives:

$$\sigma_y^2 = \sigma_a^2 + \left(1 + \frac{cf}{b^2d} + \frac{gj}{b^2h} \right)^2 \sigma_b^2 + \left(\frac{-f}{bd} \right)^2 \sigma_c^2 + \left(\frac{cf}{bd^2} \right)^2 \sigma_d^2 + \left(\frac{-c}{bd} \right)^2 \sigma_f^2 + \left(\frac{-j}{bh} \right)^2 \sigma_g^2 + \left(\frac{gj}{bh^2} \right)^2 \sigma_h^2 + \left(\frac{-g}{bh} \right)^2 \sigma_j^2 \quad (A1-15)$$

and back substitution of the definitions of (a-d, f-h, j) into A1-15 yields:

continued on next page

$$\begin{aligned}
\sigma_{\text{Pb}^*,\text{unk}}^2 &= \sigma_{\text{Pb,unk}}^2 \\
&+ \left(1 + \frac{(\text{Pb}_{\text{Th_std,200}})(\text{Th}_{\text{unk}})}{(\text{Pb}_{\text{Pb_std,10}})^2(\text{Th}_{\text{Th_std,200}})} + \frac{(\text{Pb}_{\text{Y_std,200}})(\text{Y}_{\text{unk}})}{(\text{Pb}_{\text{Pb_std,10}})^2(\text{Y}_{\text{Y_std,200}})} \right)^2 \sigma_{\text{Pb,Pb_std,10}}^2 \\
&+ \left(\frac{-\text{Th}_{\text{unk}}}{(\text{Pb}_{\text{Pb_std,10}})(\text{Th}_{\text{Th_std,200}})} \right)^2 \sigma_{\text{Pb,Th_std,200}}^2 \\
&+ \left(\frac{(\text{Pb}_{\text{Th_std,200}})(\text{Th}_{\text{unk}})}{(\text{Pb}_{\text{Pb_std,10}})(\text{Th}_{\text{Th_std,200}})^2} \right)^2 \sigma_{\text{Th,Th_std,200}}^2 \\
&+ \left(\frac{-\text{Pb}_{\text{Th_std,200}}}{(\text{Pb}_{\text{Pb_std,10}})(\text{Th}_{\text{Th_std,200}})} \right)^2 \sigma_{\text{Th,unk}}^2 \\
&+ \left(\frac{-\text{Y}_{\text{unk}}}{(\text{Pb}_{\text{Pb_std,10}})(\text{Y}_{\text{Y_std,200}})} \right)^2 \sigma_{\text{Pb,Y_std,200}}^2 \\
&+ \left(\frac{(\text{Pb}_{\text{Y_std,200}})(\text{Y}_{\text{unk}})}{(\text{Pb}_{\text{Pb_std,10}})(\text{Y}_{\text{Y_std,200}})^2} \right)^2 \sigma_{\text{Y,Y_std,200}}^2 \\
&+ \left(\frac{-\text{Pb}_{\text{Y_std,200}}}{(\text{Pb}_{\text{Pb_std,10}})(\text{Y}_{\text{Y_std,200}})} \right)^2 \sigma_{\text{Y,unk}}^2
\end{aligned} \tag{A1-16}$$

The analogous equation for corrected U precision can be written by inspection:

$$\begin{aligned}
\sigma_{\text{U}^*,\text{unk}}^2 &= \sigma_{\text{U,unk}}^2 \\
&+ \left(1 + \frac{(\text{U}_{\text{Th_std,200}})(\text{Th}_{\text{unk}})}{(\text{U}_{\text{U_std,10}})^2(\text{Th}_{\text{Th_std,200}})} \right)^2 \sigma_{\text{U,U_std,10}}^2 \\
&+ \left(\frac{-\text{Th}_{\text{unk}}}{(\text{U}_{\text{U_std,10}})(\text{Th}_{\text{Th_std,200}})} \right)^2 \sigma_{\text{U,Th_std,200}}^2 \\
&+ \left(\frac{(\text{U}_{\text{Th_std,200}})(\text{Th}_{\text{unk}})}{(\text{U}_{\text{U_std,10}})(\text{Th}_{\text{Th_std,200}})^2} \right)^2 \sigma_{\text{Th,Th_std,200}}^2 \\
&+ \left(\frac{-\text{U}_{\text{Th_std,200}}}{(\text{U}_{\text{U_std,10}})(\text{Th}_{\text{Th_std,200}})} \right)^2 \sigma_{\text{Th,unk}}^2
\end{aligned} \tag{A1-17}$$

APPENDIX 2: PROTOCOL FOR CHEMICAL AGE ANALYSIS OF MONAZITE

Calibration standards given in Table 8, preferred EMPA hardware, calibration, and analysis settings listed in Table A2-1.

1. Monazites mapped for element distribution (typically Y, Ce, Ca, Th, U, $\pm\text{Pb}$, $\pm\text{Si}$) at 200 nA, 80–100 ms dwell/pixel. Step size dependent on grain size; typically 0.5–5.0 $\mu\text{m}/\text{step}$.

2. Full quantitative analysis of desired spots performed—includes Si, P, Ca, Th, Y, Pb, U, La, Ce, Pr, Nd, Sm, Gd, Tb, Dy, Er. 15 keV, 50 nA. See Pyle (2001) for details. Note: Pb, Th, U concentrations from full quantitative analyses are too imprecise for age determination.

3. Samples (standards) given 1–4 hour finishing colloidal silica chemical-mechanical polish (CMP).

4. Samples (standards) cleaned, dried at $\sim 80^\circ\text{C}$ for 2–12 h.

5. Samples (standards) carbon coated to 200–300 \AA thickness.

6. Load samples. *Accelerating voltage set to 15 keV. *X-ray collimator slits set to open (3 mm) setting.

7. When vacuum reached desired level, saturate filament at 15 keV.

8. *Set element background collection positions (Ce, Y, U, Th, Pb) to *calibration* positions. *Check for proper detector gain, bias, baseline, and voltage window settings.

9. Locate elemental peaks on standard for each element, and perform SCA scans on each peak at 10 nA and 250 nA to ensure no voltage clipping occurs for current detector settings.

10. Perform ≥ 3 calibrations for each element at 10 nA on Faraday cup. Note large variations in initial *k*-ratio (*k*-ratio > 1.03 or *k*-ratio < 0.97) which may be caused by

- Carbon coat degradation
- Cleaning/repolishing of samples
- Faulty focus or filament saturation
- Change of or misalignment in X-ray collimators
- Previous mechanical servicing of EMPA, or new EMPA hardware

Once desired number of successful calibrations are performed, average results of selected calibrations. Calibrate lead last.

9. *Switch background collection positions to *analysis* positions.

10. Perform ≥ 5 measurements of Pb intensity on Pb standard (or, optionally, all measured elements on their respective standards) at analysis conditions (200 nA) to establish baseline for Pb calibration drift testing.

11. Perform ≥ 5 analyses of Y and Th standards to calculate average element interference correction factors for Th interference on $\text{UM}\beta$, and Th and Y interference on $\text{PbM}\alpha$.

12. (Optional) Perform one SCA scan per element, at analysis conditions, for each separate monazite compositional domain previously identified in the sample, to ensure that voltage clipping is avoided.

* Indicates EMPA-specific task.

TABLE A2-1. *Preferred EMP settings for monazite chemical age calibration and analysis

Element (spec)	crystal	gas	peak	Gain (V)	Bias (V)	Baseline (V)	Window (V)	high bkg (+mm)	low bkg (-mm)	Max Peak time (s)	Max total Background time (s)
Part I: calibration: 15 keV, 10 nA											
Y (1)	TAP	Ar	Lα	12	1725	10	70	1.20	1.60	30	30
Si (1)	TAP	Ar	Kα	12	1701	10	40	4.00	3.00	30	30
P (1)	TAP	Ar	Kα	15	1700	14	70	4.00	3.00	30	30
Ce (2)	PET	Ar	Lα	7	1700	22	70	4.00	3.00	30	30
Ca (3)	PET	Ar	Kα	6	1740	15	55	4.00	4.00	30	30
Th (3)	PET	Ar	Mα	7	1725	12	55	4.00	4.00	30	30
U (3)	PET	Ar	Mβ	6	1735	10	50	3.00	3.00	30	30
Pb4 (4)	PET	Xe	Mα	20	1800	15	30	6.27	12.73	30	30
Pb5 (5)	PET	Xe	Mα	20	1800	15	30	6.27	12.73	30	30
Part II: analysis 15 keV, 200 nA											
Y (1)	TAP	Ar	Lα	12	1725	10	70	1.20	1.60	90	90
Si (1)	TAP	Ar	Kα	12	1701	10	40	4.00	3.00	90	90
P (1)	TAP	Ar	Kα	15	1700	14	70	4.00	3.00	10	10
Ce (2)	PET	Ar	Lα	7	1700	22	70	1.20	2.20	10	10
Ca (3)	PET	Ar	Kα	6	1740	15	55	2.50	2.50	60	60
Th (3)	PET	Ar	Mα	7	1725	12	55	2.70	3.00	80	80
U (3)	PET	Ar	Mβ	6	1735	10	50	1.50(1.00)†	4.00(0.50)†	80	80
Pb4 (4)	PET	Xe	Mα	20	1800	15	30	6.27	9.05	240	240
Pb5 (5)	PET	Xe	Mα	20	1800	15	30	6.27	9.05	240	240

Notes: spec: = spectrometer number; Pb4 = lead measured on spectrometer 4, Pb5: lead measured on spectrometer 5.

* Detector settings are specific to the JEOL 733 Superprobe EMP at Rensselaer Polytechnic Institute. Background offsets are for a 140 mm Rowland circle.

† For high-Th monazite (≥15 wt%), these U background offsets may be used to mitigate the effect of the Th M4 and M5 absorption edges. However, a WD scan in the region of U Mβ should be performed to assess the intensity of the Th M4 and M5 absorption edges and their potential effect on background collection.

13. Begin analysis of unknowns. Each single analytical cycle consists of simultaneous two-spectrometer measurement of PbMα for 4 minutes on peak, and 4 minutes total on high and low background, resulting in 8 total minutes of measurement of PbMα intensity per cycle (Table 15). Spot may be re-analyzed for additional 8-minute cycles, but monitor for beam damage (reduction in absorbed current, darkening of surface). Beam size should be on the order of 5–8 μm in diameter.

14. Repeat steps 10 and 11 every 1–2 hours, or as needed, depending on severity of previously observed drift.

15. (Optional) Perform a final peak search and calibration (at calibration conditions – 10 nA) on PbMα.

16. If a significant deviation from the initial Pb *k*-ratio occurs during analysis [as shown by results of repeated (10,11)], regress Pb *k*-ratio against time so that a relation of the form

$$k\text{-ratio}_{\text{Pb std}}(t) = mt + k\text{-ratio}_{\text{Pb std}}(t_0)$$

is generated, where *m* is the slope of the regression line relating time and Pb *k*-ratio, and $k\text{-ratio}_{\text{Pb std}}(t_0)$ is the initial Pb standard *k*-ratio. If the drift appears continuous, one regression line is calculated, and if the drift appears to have been punctuated, the regression line is divided into the appropriate number of segments. For the time *t* of each unknown point analysis, $k\text{-ratio}_{\text{Pb std}}(t)$ is calculated, the percentage change from the initial Pb standard *k*-ratio is calculated, and the unknown Pb *k*-ratio is multiplied by that factor. The drift corrected *k*-ratios are again *ZAF— or φρz-corrected.

17. If no drift of Pb calibration is apparent, correct for Th interference on UMβ and Th + Y interference on PbMα by use of Equations A1-3a and A1-3b, using correction factors measured on standards throughout the analytical session, and unknown *k*-ratios of Th and Y from individual unknown analyses.

For analysis of sample T22 performed on 13 February 2003, calibration information is given in Table 14. Three calibrations were performed on Y, Ce, and Th standards, U was calibrated 4 times, and Pb4 and Pb5 were calibrated 5 times. After initial

measurement of Pb *k*-ratio at 200 nA (Figs. 21b and 21c), correction factors were measured for Y and Th interference on PbMα (Table 16). During this analytical session, three blocks of unknown monazites were analyzed; T22 was the second of three blocks to be analyzed, and analysis required approximately 6 hours for 50 spot analyses. Five measurements of Pb standard *k*-ratio were made each on spectrometers 4 (Fig 21b) and 5 (Fig. 21c), immediately before and after the T22 analysis block, and these two *k*-ratio measurements formed part of a group of four measurements from which a linear correction for time-dependent spectrometer drift was generated:

$$\text{Pb4}_{k\text{-ratio},t} = 0.0078(\text{time}) + 1.0103 \quad (\text{A2-1a})$$

$$\text{Pb5}_{k\text{-ratio},t} = -0.1887(\text{time}) + 0.9995 \quad (\text{A2-1b})$$

After a fictive lead *k*-ratio at time *t* (analytical time) is calculated, the drift-corrected lead concentration is calculated as:

$$\text{Pb4}_{\text{corr},t} = \text{Pb4}_{\text{uncorr},t} * (\text{Pb4}_{k\text{-ratio},t} / \text{Pb4}_{k\text{-ratio},t_0}) \quad (\text{A2-2a})$$

$$\text{Pb5}_{\text{corr},t} = \text{Pb5}_{\text{uncorr},t} * (\text{Pb5}_{k\text{-ratio},t} / \text{Pb5}_{k\text{-ratio},t_0}) \quad (\text{A2-2b})$$

where $\text{Pb4}_{k\text{-ratio},t_0} = 1.0103$ and $\text{Pb5}_{k\text{-ratio},t_0} = 0.9995$. For the drift correction factor measured in this analytical session, lead concentrations on spectrometer 4 increase less than 1% over the analysis interval, but decrease 2–6% on spectrometer 5 over the analysis interval.

Once drift-corrected lead concentrations are calculated, Pb concentrations are corrected, according to Equation A1-3a and for Th ($M\zeta_{1,2}$, $M2-O4$) and $YL\gamma_{2,3}$ interference, using the correction factors listed in Table 15, and U is corrected for $ThM\gamma$ interference using Equation A1-3b using the correction factor listed in Table 15. Corrected U and Pb concentrations are inserted, along with Th concentration, into Equation 1 (Montel et al. 1996), and that equation is solved iteratively for time, using the Microsoft Excel goal seek routine set to a maximum of 10000 iterations, with a tolerance of 1×10^{-6} .